Earth's Cryosphere Albedo Feedback: from the Global Scale to Snow Metamorphosis

by

Adam M. Schneider

A dissertation submitted in partial fulfillment
of the requirements for the degree of
Doctor of Philosophy
(Atmospheric, Oceanic, and Space Sciences)
in The University of Michigan
2018

Doctoral Committee:

Associate Professor Mark Flanner, Chair
Associate Research Scientist Roger De Roo
Associate Professor Xianglei Huang
Assistant Professor Branko Kerkez

Adam M. Schneider

amschne@umich.edu

ORCiD: 0000-0002-8760-1639

For my family

ACKNOWLEDGEMENTS

This work is funded, in part, by the National Science Foundation, grant number ARC-1253154.

We acknowledge the World Climate Research Programme's Working Group on Coupled Modeling, which is responsible for CMIP, and we thank the climate modeling groups (listed in Table 1 of Chapter 2) for producing and making available their model output. For CMIP the U.S. Department of Energy's Program for Climate Model Diagnosis and Inter-comparison provides coordinating support and led development of software infrastructure in partnership with the Global Organization for Earth System Science Portals.

We wish to thank two anonymous reviewers for taking time to read Chapter 2 and for providing helpful comments.

I would like to thank colleagues at the Cold Regions Research and Engineering Laboratory (CRREL) in Hanover, New Hampshire for their generous support. In particular, thanks to Zoe Courville and John Fegyveresi for their hospitality and guidance navigating the facilities at CRREL. I also want to thank Ross Lieblappen for sharing his micro-computed tomography expertise through providing a thorough tutorial for running and analyzing snow scans. Finally, thanks to Alden Adolph for facilitating travel accommodations and welcoming me to Hanover, New Hampshire in 2016 and 2017.

To my advisor, Professor Mark Flanner, thank you for offering limitless guidance, mentorship, and support throughout the last six years. Under your direction, I de-

veloped a mathematics background into a scientific arsenal of problem solving skills. Throughout our countless discussions, I learned how to think scientifically, seek a physical understanding of underlying concepts, and communicate to experts in our field. I was always thrilled to carry out your brilliant ideas and am grateful for the life changing opportunity you provided me. Looking back on my time at the University of Michigan, it is difficult to outline even the topics that cover all the material I learned while studying atmospheric, climate, and cryospheric sciences. You afforded me the opportunity to pursue my academic passions and supported my studies even when they served my self interests. I cannot imagine working with another mentor as closely as I worked with you. I will undoubtably miss our current professional and friendly relationship, but also look forward to pursuing our common interests in the future. Thank you.

To my brother and life-long assistant, Jordan Basil Schneider, thank you for providing tremendous guidance on my journey to becoming a scientific programmer. Undoubtedly, I have come a long way since those long Python programming sessions at Shapiro, Espresso Royale, and several other locations throughout Ann Arbor offering free internet access. I have no doubt that I would not have accomplished much of the work leading to this dissertation without your patient, expert support throughout the years.

Finally, to my loving mother Nancy Jo Chryssos, thank you for providing endless love and support. You have given me twenty-nine years and nine months of continuous, unconditional mental, emotional, and financial assistance that has resulted in the culmination of an aspiring scientist. Your guidance, motivation, and loving words of encouragement always enables tough times to become less so; challenging tasks to seem doable. You are my biggest fan (maybe second, only to Maya or Gary), and simply put, I would not be the man I am today without your inspiration and necessary involvement in my life. Thank you, love Adam.

TABLE OF CONTENTS

LIST OF FIGURES

Figure

LIST OF TABLES

Table

LIST OF APPENDICES

Appendix

ABSTRACT

Previous studies report rapid perennial Arctic sea ice-cover decline over the last few decades, but decadal-scale temporal variability of Earth's albedo feedback has not been fully assessed in future climate simulations. Without a complete dynamic treatment of albedo feedback on these timescales, a question that motivates the research presented here is how does the strength in albedo feedback vary on decadal timescales in transient climate? The answers to when the strength in albedo feedback might peak and start to decline in future transient climate simulations is the topic of Chapter 2. On smaller scales, snow internal albedo feedback is a poorly understood source of instability in snowpacks that can affect the surface energy budget. Mechanisms for both positive and negative snow metamorphosis-driven albedo feedback have been proposed, but due to the delicate nature of snowpacks, it can be difficult to study these mechanisms in nature. Chapters 3 and 4 seek to better understand the snow internal albedo feedback on hourly timescales.

Data from the Coupled Model Intercomparison Project Phase 5 (CMIP5) multi-model ensemble of simulations of historical and future transient climate is applied to assess global scale surface albedo feedback (SAF) in 36 global climate models. Time evolving SAF in multiple decades are calculated from surface albedo and temperature linear regressions. Results are meaningful when temperature change exceeds 0.5K. Decadal scale SAF is strongly correlated with century scale SAF during the 21st century. Throughout the 21st century, multi-model ensemble mean SAF increases from 0.37 to 0.42 watts per square meter Kelvin. These results suggest models' mean decadal scale SAFs are good estimates of their century scale SAFs if there is at least

0.5K temperature change. Persistent SAF into the late 21st century indicates ongoing capacity for Arctic albedo decline despite there being less sea-ice.

To examine the snow internal albedo feedback, first, an instrument designed to measure snow specific surface area (SSA) is engineered to operate in situ during subfreezing conditions. To calibrate the Near-Infrared Emitting and Reflectance-Monitoring Dome (NERD), measured bidirectional reflectance factors (BRFs) are compared to snow SSA estimates derived from X-ray microcomputed tomography (X-CT) scans. This comparison contains multiple snow samples of various morphological quantities including snow density, porosity, and SSA ranging from 10 to 70 square meters per kilogram. In general, there is an exponential relationship between 1.30 micro-meter BRFs and snow SSA. These results provide experimental validation of measuring 1.30 micro-meter BRFs to obtain approximate snow SSA.

Second, two NERDs are deployed to measure 1.30 and 1.55 micro-meter BRFs of natural snow and experimental snow plots with added dust and BC. Snow 1.30 (1.55) micro-meter BRFs evolve from 0.6 (0.15) in fresh snow to 0.2 (0.03) after metamorphosis. Hourly-scale time evolving snow surface BRFs and SSA estimates from X-CT reveal more rapid infrared darkening and snow metamorphosis in contaminated versus natural plots. These findings verify experimentally that dust and BC deposition can accelerate snow metamorphosis and enhance positive snow internal albedo feedback in sunny, calm weather conditions.

CHAPTER I

Introduction: From Climate and Radiative Transfer Models to Engineering and Snow Science

1.1 Background

1.1.1 Reflectance Terminology

The most elementary definition of the term *reflectance* describes the percentage of incident radiative energy that is redirected back into the hemisphere from where it originated. It is purely a ratio of the light a surface reflects and has nothing to do with light emission. Therefore, conservation of energy requires that reflectance values range from 0 to 1. More precisely, this description of reflectance is better defined as biconical reflectance. Because of the highly directionally dependent nature of radiative energy transfer, reflectance definitions and measurements are inherently complicated. Biconical reflectance of an infinitesimal surface element with area dA and with negligible subsurface scattering is defined as the ratio of the amount of reflected radiant energy into an arbitrarily large solid angle to that of the incident radiant energy on the surface from another arbitrarily large solid angle. When these solid angles increase to 2π steradians, or the total solid angle of a hemisphere, the percentage of reflected radiant energy from the infinitesimal surface element is called bi-hemispherical reflectance. Bi-hemispherical reflectance is a convenient description

of a surface in the plane-parallel context. It is defined as the percentage of radiant energy incident from an entire hemisphere reflected back into the hemisphere. In radiative transfer modeling using the two-stream approximation, bi-hemispherical reflectance sufficiently describes the reflectance of a plane-parallel layer. On the other hand, when the biconical reflectance solid angles become infinitesimally small, instead of defining the percentage of total radiation that is reflected to and from the entire hemisphere, bidirectional reflectance then fully describes the angular dependence of reflectance of light from the surface element (*F.E. Nicodemus et al.*, 1977; *Painter et al.*, 2009; *Hudson et al.*, 2006; *Dumont et al.*, 2010).

Bidirectional reflectance, defined by both incident and reflected angles, is a more complete description for the reflective properties of a surface. The most complete description of the reflectance of a surface element, however, is known as the bidirectional reflectance distribution function. Accounting for subsurface scattering of light beneath the surface element, the bidirectional scattering-surface distribution function gives the entire description of the reflectance of light from any arbitrary surface. These full descriptions of reflectance, however, are almost purely theoretical and extremely difficult to measure. Measuring absolute reflectance is also challenging. Because of these challenges, observationalists often find it convenient to measure reflectance factors (*F.E. Nicodemus et al.*, 1977; *Painter et al.*, 2009; *Hudson et al.*, 2006; *Dumont et al.*, 2010).

Hemispherical-, conical- and directional- prefixes that define different types of reflectances are also valid in specific descriptions of reflectance factors. For all of these prefixes, a reflectance factor defines the ratio of reflected light into an entire hemisphere, arbitrarily large solid angle, or infinitesimally small solid angle with precise angular dependence, compared to that of a perfect Lambertian surface with constant bidirectional reflectance for all incident and viewing angles of 1. This ideal surface reflects all light from all directions perfectly isotropically according to Lambert's cosine

law. This implies that this idealized surface is equally bright for all viewing angles. These surfaces, though rare in nature, are used as calibration standards in reflectance factor measurements. Observationalists measure reflectance factors by dividing radiant energy fluxes measured over surfaces of interest by radiant energy fluxes measured over an idealized Lambertian surface. Unlike reflectance values, reflectance factors range from 0 to infinity. In contrast to Lambertian reflection, where incident light is reflected perfectly isotropically, specular reflection yields reflectance factors higher than 1 as reflected light is contained within a single direction. In the event that a Lambertian surface is not a perfectly lossless (i.e., has a bidirectional reflectance of less than 1), measuring reflectance factors then requires knowledge of the Lambertian surface reflectance to scale the quotients accordingly (*F.E. Nicodemus et al.*, 1977; *Painter et al.*, 2009; *Hudson et al.*, 2006; *Dumont et al.*, 2010).

The following sections and later chapters make frequent use of the following terms: albedo, directional-hemispherical reflectance, and bidirectional reflectance factors (BRFs). In the case of albedo feedback, almost all mentions of the term albedo on the global scale refer to directional-hemispherical reflectance. Directional-hemispherical reflectance (also known as black-sky albedo) refers to the percentage of directionally dependent incident radiation that is reflected back into the upward facing hemisphere. In the context of planetary albedo, for example, black-sky albedo is appropriate as the sun represents the primary light source from a specific direction. Directional-hemispherical reflectance then best describes the planetary albedo as light from other directions (space) is minimal and solar radiation is reflected by Earth into all directions in the hemisphere. Earth's surface albedo, however, is slightly more complicated. In a cloud free atmosphere, Rayleigh scattering of blue light by Earth's atmosphere is responsible for diffuse illumination of the surface. In this case, surface albedo is best described by the combination of its directional-hemispherical reflectance, angularly defined by the solar zenith angle, and bi-hemispherical reflectance

of blue light. Under overcast, multiple-scattering of light within clouds results in surface illumination that is nearly isotropic. In this case surface albedo is well approximated by bi-hemispherical reflectance, hence the name white-sky albedo.

Finally, in chapters 3 and 4, understanding of the term BRF is paramount. To reiterate, BRFs must have angularly dependent light sources and viewing angles. They also must be related to Lambertian surfaces as they are a comparative quantity. Comparative quantities are usually easier to obtain through measurements than absolute quantities and will be useful throughout this dissertation.

1.1.2 Earth's Planetary Energy Budget

The law of conservation of energy states that in an isolated system, energy is neither created nor destroyed. This implies that the transfer of energy into and out of the system determines the total energy budget. The transfer of energy can occur through conduction, convection, phase changes, and through the propagation of electromagnetic waves. The propagation of electromagnetic waves, i.e., radiative transfer, is the primary form of energy transfer in a vacuum. Because the planet Earth is surrounded by a vacuum, negligible mass transfer from extraterrestrial objects implies that nearly all of the energy exchange into and out of the Earth system is through radiative transfer.

Applying the law of conservation of energy to the Earth system as an isolated object in space, the primary source of energy into the Earth system is absorbed solar radiation. Absorbed solar radiation by the Earth is represented mathematically in terms of the solar luminosity L_0, planetary albedo α_p, and Earth's radius r_p and distance from the sun d, such that

$$a_p Q = \frac{L_0}{4d^2}(1 - \alpha_p) r_p^2, \tag{1.1}$$

where a_pQ represents the total solar energy flux incident at the top of the atmosphere (TOA) times the planetary absorptivity (co-albedo) with $a_p = 1-\alpha_p$. L_0 is essentially the radiative power output of the sun and is approximately 3.9×10^{26} W. The sun's radiative power output through a finite surface element defines the solar irradiance and is well approximated by blackbody radiation laws for an emission temperature of 5800K. Dividing L_0 by $4\pi d^2$ gives the solar irradiance at a distance d in a vacuum. At a mean distance from the sun of 1.496×10^{11}m, this quotient gives the solar constant S_d relevant to Earth for which *Kopp and Lean* (2011) report a recent estimate of 1360.8 +/- 0.5 Wm^{-2}. Multiplying the solar constant by the projected area of the Earth (πr_p^2) gives the total solar energy flux incident at the Earth's TOA (Q). Finally, Earth's planetary albedo α_p is defined as the ratio of the total absorbed solar energy to the total solar energy incident at the TOA. The planetary co-albedo a_p thus scales the total solar energy flux to give the absorbed solar energy flux as in equation 1.1 (*North and Kim*, 2015).

Because the solar luminosity and Earth's mean distance from the sun, radius, and planetary albedo are all relatively constant, the law of conservation of energy implies that the Earth system in equilibrium must emit radiation equal in total power output to that of the total absorbed solar radiation given by equation 1.1. Stefan-Boltzmann's law then gives Earth's energy balance equation in terms of its brightness temperature T_B and emissivity ϵ such that

$$\frac{a_p S_d}{4} = \epsilon \sigma T_B^4, \tag{1.2}$$

where σ is the Stefan-Boltzmann constant equal to 5.67×10^{-8} $\mathrm{Wm}^{-2}\mathrm{K}^{-4}$. *Budyko* (1969) and *Sellers* (1969) apply these principles of Earth's energy balance in a class of simple global climate models to assess glaciation and climate change sensitive to subtle variations in absorbed solar radiation. In these models, absorbed solar radiation varies

as volcanic eruptions and changes in the solar constant allow for changes in Earth's planetary energy budget. *Donohoe and Battisti* (2011) demonstrate that Earth's planetary albedo is primarily dependent on atmospheric attenuation of solar radiation. Clouds are responsible for reflecting a significant portion of the TOA solar irradiance back to space. This cloud masking of the surface minimizes the dependency of Earth's planetary albedo on its surface albedo. At high latitudes, however, Earth's highly reflective ice covered polar regions enable a stronger contribution of surface albedo on the planetary albedo. High latitude surface albedo contribution to planetary albedo can enhance climate change via the snow and ice albedo feedback.

1.1.3 Ice Albedo Feedback and Arctic Climate Change

The ice albedo feedback is a positive feedback mechanism operating in transient climate. In global warming, for example, increasing surface temperature at the ice boundary latitude results in the removal of snow and ice covered surfaces as temperatures exceed zero degrees Celsius (°C) (*Held and Suarez*, 1974; *North*, 1975). Because ice cover is most often much more reflective in the solar spectrum than its underlying surface, large scale changes from ice cover to ice free surfaces result in a large decrease in the surface albedo. Depending on the atmospheric conditions relating to cloud masking of the surface, these changes in surface albedo are propagated to the TOA. When these changes occur on large scales, as is the case in recent summer Arctic sea-ice area trends (*Cohen et al.*, 2014), the planetary albedo is affected negatively. This directly increases the absorbed solar radiation. Because the total energy content of the planet cannot grow boundlessly, the equilibrium response to increased absorbed solar energy results in an increase in the Earth's blackbody emission temperature. The change in Earth's equilibrium global mean surface temperature in response to a radiative forcing is determined by Earth's climate sensitivity. Earth's climate sensitivity is a function of its fundamental climate feedbacks. These include

temperature, albedo, water vapor, and cloud feedbacks (*Dessler*, 2013; *Soden and Held*, 2006). Stronger temperature and albedo feedbacks at higher latitudes are primary contributors of amplified Arctic climate change (*Pithan and Mauritsen*, 2014).

Highly reflective sea-ice cover characterizes Earth's polar regions' surface energy budget. In transient climate, ice albedo feedback is a likely contributor of the widely reported amplification of Arctic climate change. Amplification of Arctic climate change is the more rapid increase of surface temperatures in northern high latitudes compared to the global mean. In addition to the rapid reduction of perennial Arctic sea-ice cover, amplification of Arctic climate change is evidenced by surface temperatures warming at a rate three times faster than that of the global average since 1980 (*Comiso*, 2012). Perennial Arctic sea-ice cover consists of multi-year ice that persists throughout the entire annual cycle. Minimum Arctic sea-ice extent occurs during the month of September as the North polar region transitions from late summer to complete darkness during the winter months. *Stroeve et al.* (2007) show that global climate models from the Intergovernmental Panel on Climate Change Fourth Assessment Report underestimate on average September Arctic sea ice decline since 1950. *Comiso et al.* (2008) and *Cavalieri and Parkinson* (2012) apply microwave satellite observations to confirm the rapid reduction in perennial Arctic sea-ice cover since 1980. In addition to the rapid reduction of perennial Arctic sea-ice, submarine based sonar data and laser altimetry from the Ice, Cloud, and and Elevation Satellite (ICESat) suggest sea-ice thickness in various regions of the Arctic is also declining rapidly since 1958 (*Kwok and Rothrock*, 2009).

Modern advances in satellite and remote sensing technology enables observational determination and verification of Arctic climate change. *Pistone et al.* (2014), for example, apply The Clouds and Earth's Radiant Energy System (CERES) satellite data to directly link diminishing Arctic sea-ice cover to decreasing Arctic planetary (TOA) albedo. They also conclude that changes in cloud cover have a minimal im-

pact on the albedo decline. This finding highlights the importance of the diminishing surface albedo in the Arctic energy budget. Furthermore, *Flanner et al.* (2011) apply data from the Moderate Resolution Imaging Spectroradiometer (MODIS) and determine that the instantaneous net TOA radiative energy perturbation caused by the presence of snow and / or ice (also known as the cryosphere radiative effect (*Perket et al.*, 2014)) declined by an average of 0.45 Wm^{-2} in the northern hemisphere from 1979-2008. This decline represents an increase in absorbed solar radiation directly resulting from decreasing snow and ice cover over the 30 year measurement period.

The dramatic negative trend in Arctic perennial sea-ice cover is certainly notable. Recent studies demonstrate its consequential effect on Arctic climate. Additionally, from a global climate perspective, the vast Arctic sea-ice coverage potentiates a large climate change response. Another source of albedo feedback in modern climate change, however, is decreasing snow cover extent (SCE).

Dery and Brown (2007) show declining trends in northern hemisphere springtime SCE over the period of 1972-2006. Like in ice albedo feedback, earlier onset of springtime snow melt over broad regions increases absorbed solar energy through the reduction of surface albedo. Reduced surface albedo due to these trends enables positive snow albedo feedback in both climate change and seasonal cycle contexts. *Hall and Qu* (2006) show in climate models that the strength in northern hemisphere springtime snow albedo feedback is highly correlated across seasonal and climate change contexts. In the seasonal cycle, snow albedo feedback affects the timing of snowmelt especially over northern hemisphere extra-tropical land masses (*Qu and Hall*, 2014). This periodically occurring feedback that accelerates snowmelt during spring also accelerates climate change on decadal timescales.

Recent review articles highlight the important role SCE has in Arctic and high altitude regional climate (*Cohen et al.*, 2014; *Mountain Research Initiative EDW Working Group*, 2015). Because of its high reflectivity, like ice, snow cover has a large

impact on the surface energy budget. Direct solar irradiance can initiate powerful positive snow albedo feedback through enhanced energy absorption at the surface. Furthermore, light absorbing impurities (LAI) within snowpacks can amplify albedo feedback resulting in enhanced snow metamorphosis. This internal feedback can increase snowmelt rates in regions with high concentrations of LAI. In the Colorado river basin, for example, episodic dust deposition directly reduces snow albedo (*Skiles and Painter*, 2017) . Indirectly, enhanced absorption by LAI at the snow surface triggers positive albedo feedback, enhances snow metamorphosis, and increases melt rates which can affect water resource management. Furthermore, as snow cover is removed through these processes, darker surfaces with lower reflectances are exposed. Uncovered surfaces of lower albedo further enhances absorbed solar irradiance and drives positive albedo feedback.

1.2 Research Objectives and Theses

Due to the significant discrepancy in observable Arctic sea-ice cover decline and that predicted in global climate models there is an ongoing demand for decadal-scale climate modeling evaluation. *Wang and Overland* (2012) evaluate Arctic sea-ice decline in seven climate models participating in the CMIP5 and find that summer Arctic sea-ice nearly vanishes by 2030 in future climate simulations under the RCP8.5. It is unclear how the rapid diminishing Arctic sea-ice extent will affect surface albedo feedback. With there being less perennial sea-ice cover in the models, we expect SAF to decrease throughout the twenty-first century and beyond. Until now, without decadal-scale evaluation of this feedback, it is unclear when the strength of the feedback will peak, decline, and eventually vanish as all snow cover and Arctic sea-ice is melted out of models. The Coupled Model Inter-comparison Project Phase 5 (CMIP5) provides a class of coupled global climate models capable of simulating transient future climate with various greenhouse gas emissions scenarios known as the

Representative Concentration Pathways (RCPs). Greenhouse gas concentration radiative forcings of 2.6, 4.5, 6.0, and 8.5 Wm^{-2} by the year 2100 define these scenarios. These radiative forcings are estimated based on a wide range of possible emissions scenarios with the RCP8.5 considered the "business as usual" case, where little to no significant intervention of greenhouse gas emissions results in minimal climate change mitigation throughout the 21st century.

To inform decadal-scale climate projections from global climate models, chapter 2 evaluates surface albedo feedback (SAF) on decadal timescales to explore variability in the strength of feedback. To our surprise, CMIP5 simulations under the RCP8.5 scenario show no signs of systematic SAF weakening throughout the 21st century. Instead, multi-model mean SAF significantly, though marginally, strengthens throughout the 21st century. Extended simulations carried out through 2300 suggest SAF peaks in the 22nd century, after which it declines monotonically as it approaches zero.

Another desirable improvement in current global climate modeling is better representations of LAI in snow processes that enrich the snow aging process. Because of the strong dependence of snow albedo (especially in the infrared) on snow grain size, snow aging processes that result in increasing snow grain size can initiate positive albedo feedback within the snow. While the direct darkening effects of LAI on snow are well-represented in todays snow albedo models (e.g. SNICAR), indirect darkening via positive albedo feedback through snow aging is crudely approximated.

To help inform on the effects of LAI on snow metamorphosis, we first engineer an instrument capable of obtaining approximate snow specific surface area (SSA) in the field. In designing a light-weight, portable instrument operational down to -20° Celsius, we are able to study hourly scale snow metamorphosis in the field. Chapter 3 details the design principles and instrument validation of the Near-Infrared Emitting Reflectance and Monitoring Dome (NERD) used to measure snow SSA. In Chapter

4, we then apply the NERD in LAI-in-snow experiments to study the enhancement of snow metamorphosis due to the presence of LAI. As expected, we find that under direct solar illumination of the snow in near, but below, freezing surface temperatures, added LAI in snow rapidly initiates positive internal snow albedo feedback. Just a small amount (<1 to 30g) of added LAI is needed to drive visibly apparent changes in the snow surface state. These experiments represent some of the first of its kind demonstrating in situ the powerful indirect effects of LAI in snow on hourly timescales.

CHAPTER II

Multidecadal Variability in Surface Albedo Feedback Across CMIP5 Models

As published in:

Schneider, A., M. Flanner, and J. Perket (2018), Multidecadal Variability in Surface Albedo Feedback Across CMIP5 Models, *Geophysical Research Letters, 45*(4), 1972−1980, doi:10.1002/2017GL076293.

Abstract:

Previous studies quantify surface albedo feedback (SAF) in climate change, but few assess its variability on decadal timescales. Using the Coupled Model Intercomparison Project Version 5 (CMIP5) multi-model ensemble dataset, we calculate time evolving SAF in multiple decades from surface albedo and temperature linear regressions. Results are meaningful when temperature change exceeds 0.5K. Decadal scale SAF is strongly correlated with century scale SAF during the 21st century. Throughout the 21st century, multi-model ensemble mean SAF increases from 0.37 to 0.42 $\mathrm{Wm^{-2}K^{-1}}$. These results suggest models' mean decadal scale SAFs are good estimates of their century scale SAFs if there is at least 0.5K temperature change. Persistent SAF into the late 21st century indicates ongoing capacity for Arctic albedo decline despite there being less sea-ice. If the CMIP5 multi-model ensemble results are representative of the Earth, we cannot expect decreasing Arctic sea-ice extent to

suppress SAF in the 21st century.

2.1 Introduction

Radiative transfer is the primary phenomenon governing energy exchange between Earth and the surrounding vacuum. Therefore, Earth's total energy budget is well approximated by the difference in absorbed solar and emitted terrestrial radiation at the top of the atmosphere (TOA). Simple energy balance models use the TOA approximation to demonstrate enhanced climate sensitivity from surface albedo feedbacks. *Budyko* (1969) and *Sellers* (1969), for example, find that relatively small changes in incident solar radiation coupled with changes in planetary albedo can cause glaciation or deglaciation of the planet in climate models, identifying snow and ice albedo feedback as a possible mechanism for instability in the climate state. The snow and ice albedo feedback is a positive feedback that accelerates climate change when increasing (decreasing) temperature causes snow and ice cover to decrease (increase), reducing (enhancing) albedo and further enhancing surface warming (cooling). Because snow and ice are often much brighter than their underlying surfaces, the high albedo contrast potentiates snow and ice albedo feedbacks to amplify Arctic climate change where increasing temperatures reduce surface albedo and accelerate melt. *Qu and Hall* (2014) examine Northern Hemisphere snow albedo feedback in Coupled Model Inter-comparison Project Version 5 (CMIP5) models and show a strong correlation between feedback in the spring time melting season and feedback in climate change. This correlation suggests the seasonal cycle Northern Hemisphere snow albedo feedback derived from remote sensing observations can constrain the climate change feedback in models. *Crook and Forster* (2014), however, find discrepancies between Northern Hemisphere surface albedo feedback (SAF) in the climate change and seasonal cycle contexts when comparing observations to models. These results cast doubt on the predictive capability of the seasonal cycle SAF as it relates to

the climate change feedback. Constraining SAF in climate models is important for improving the accuracy of climate change predictions from inter-comparison projects cited frequently by the Intergovernmental Panel of Climate Change (IPCC) reports. The IPCC fifth assessment report (*Flato et al.*, 2014), for example, cites numerous studies showing drastic reductions in summer Arctic sea ice extent by 2100 in CMIP5 models. This reduction in Arctic sea-ice impacts Earth's total energy budget and amplifies climate change via the SAF.

Pistone et al. (2014) and *Cao et al.* (2015), for example, relate the recent decline in observed planetary albedo directly to the loss of Arctic sea-ice cover. Rapid Arctic sea-ice loss and rising surface temperatures are characteristic of transient future climate simulations under the 8.5 Wm^{-2} greenhouse gas radiative forcing Representative Concentration Pathway (RCP8.5). *Hall* (2004) demonstrates in a coupled atmosphere-ocean model simulation that SAF enhances both polar amplification of surface temperature anomalies and surface temperature at all latitudes in the equilibrium response to CO_2 doubling. *Winton* (2006a) and *Pithan and Mauritsen* (2014) find SAF to be a secondary driver of polar amplification, however, citing temperature feedbacks as the primary contributor. In a consistent evaluation of global climate feedbacks in coupled atmosphere-ocean climate models, *Soden and Held* (2006) find SAF the third strongest positive feedback in current climate after water vapor and cloud feedbacks. *Winton* (2006b) reports a multi-mean SAF of 0.3 $\mathrm{Wm}^{-2}\mathrm{K}^{-1}$ in the IPCC fourth assessment climate models. Other studies quantify snow and SAF in global climate models (*Qu and Hall*, 2006, 2007; *Fletcher et al.*, 2012; *Vial et al.*, 2013; *Crook and Forster*, 2014; *Qu and Hall*, 2014; *Andry et al.*, 2017) and from remote sensing observations (*Hall and Qu*, 2006; *Fernandes et al.*, 2009; *Flanner et al.*, 2011; *Hudson*, 2011; *Fletcher et al.*, 2012; *Qu and Hall*, 2014; *Fletcher et al.*, 2015). *Andry et al.* (2017) examine time dependent variations in SAF in six CMIP5 models using a moving window technique. Here, we use a similar technique to expand on

previous analyses in 36 CMIP5 models to address the following.

As Arctic sea-ice continues to melt, we expect SAF to weaken as less highly reflective snow and ice remains to allow large changes in albedo. The onset of 21st century SAF weakening is unclear, however, as nearly all previous studies do not resolve the time-dependency of SAF. In calculating climate change SAF on multiple decadal timescales, we evaluate its temporal evolution and identify when and if weakening occurs. Allowing SAF to vary on decadal time scales also allows for testing its predicative capability of models' longer, century-scale feedback. In comparing multiple models' decadal timescale feedbacks to their century-scale feedbacks, we can also evaluate how well remote sensing products, limited in duration by the satellite era, may be able to constrain longer timescale climate change SAF. In this paper, we present a new technique for calculating time evolving SAF in 36 CMIP5 models in transient historical and future climate simulations ranging from 1850-2300. Contrary to our initial expectations, we discover small but significant strengthening of SAF throughout the 21st century in most CMIP5 climate models.

2.2 Methods and Data

SAF is defined as the change in global mean net TOA shortwave irradiance caused by the change in surface albedo per global mean surface temperature change. It can be expressed mathematically in the following form (*Hall*, 2004; *Winton*, 2006b; *Colman*, 2013; *Crook and Forster*, 2014),

$$\text{SAF} = \frac{\partial Q_{net}}{\partial \alpha_S} \frac{\Delta \alpha_S}{\Delta T_S}, \tag{2.1}$$

where $\partial Q_{net}/\partial \alpha_S$ is the radiative kernel and $\Delta \alpha_S$ and ΔT_S are surface albedo and surface temperature changes, respectively. Global mean temperature change is used in this study instead of hemispheric or zonal means enabling direct comparisons to

other climate feedbacks.

SAF is calculated over separate 11, 23, 47, and 94-year time periods within the CMIP5 multi-model ensemble simulations in transient historical and future climate under the RCP8.5. These time periods are selected to maximize the number of samples within the 21st century for decadal, quarter century, half century, and full century scale SAF between 2006 and 2099. The CMIP5 multi-model ensemble dataset contains monthly mean surface upwelling and downwelling irradiance used to calculate grid-cell albedo and annual global mean surface temperature (*Taylor et al.*, 2012). Monthly grid-cell albedo and annual global mean temperature are used to compute 11, 23, 47, and 94-year changes in grid-cell albedo by month and global mean temperature using least squares regressions.

Because least squares regressions are particularly sensitive to outliers, yearly grid-cell albedo by month and global mean temperature time series are first run forwards and backwards through a low-pass Butterworth filter using the convolution theorem. The low-pass Butterworth filter is defined by the power gain in terms of its transfer function (*Roberts and Roberts*, 1978),

$$|H_B(j\omega)|^2 = \left[1 + \frac{\tan(\omega T/2)}{\tan(\omega_c T/2)}\right]^{-2n}. \tag{2.2}$$

The discrete transfer function H_B gives the complex frequency domain response and is specified by the sampling interval T, corner-frequency ω_c, and order of the filter n. With $T = 1$ year, $n = 1$ and $\omega_c = 1/11$ years^{-1} are selected to damp high frequency signals associated with dynamical modes in the climate system. The El Nino / La Nina Southern Oscillation, for example, can cause short term fluctuations in both albedo and temperature output that obscure long term trends and needlessly affect least squares regressions. After filtering, least squares regressions are computed on filtered grid-cell albedo by month and global mean temperature time series to give

the 11, 23, 47, and 94-year changes.

Grid-cell albedo changes for each month are then multiplied by two monthly resolved radiative kernels to give the TOA change in net irradiance caused by the albedo change. This method is introduced by *Shell et al.* (2008) and *Soden et al.* (2008) and enables the quantification of SAF in transient climate for a fixed cloud field. Using a fixed cloud field invariant in time is useful here as it allows for direct comparisons of SAF across models independent of their transient atmospheric conditions and cloud feedbacks. The two radiative kernels used in this study are calculated from the Geophysical Fluid Dynamics Laboratory (GFDL) Atmosphere Model (AM2) (*Soden et al.*, 2008) and the Community Earth System Model (CESM1) Community Atmosphere Model (CAM5).

Finally, annual global means are calculated from the 11, 23, 47, and 94-year changes in grid-cell TOA net irradiance. These changes are divided by the respective 11, 23, 47, and 94-year changes in global mean temperature. The resulting quotients give the 11, 23, 47, and 94-year global mean SAF as defined in equation 1. SAF is calculated in this manner for the 36 models listed in Table 1 using the CMIP5 multi-model ensemble output.

2.3 Results and Discussion

Equation 1 shows there is no limit to SAF as the change in global mean surface temperature approaches zero. Figure 1 demonstrates the consequences of this limitless behavior in the calculation of SAF. We scatter SAF against the change in global mean surface temperature in 11, 23, 47, and 94-year windows across all historical and future simulations from models listed in Table 1 using both the CAM5 and AM2 radiative kernels. SAF is noisy when temperature change is less than roughly 0.5K. This temperature change threshold exists for all window lengths, suggesting that at least 0.5K warming (or cooling) is necessary to calculate meaningful SAF in climate change.

CMIP5 21st century- and decadal- scale SAF ($Wm^{-2}K^{-1}$)

Model Name	2006-2099	2006-2028	2075-2097	23-yr. STD
ACCESS1.0	0.39	0.51	0.44	0.07
ACCESS1.3	0.36	0.14	0.44	0.13
BCC-CSM1.1	0.40	–	0.51	0.11
BCC-CSM1.1(m)	0.29	0.27	0.48	0.12
BNU-ESM	0.61	0.60	0.48	0.09
CanCM4*	–	–	–	–
CanESM2	0.36	0.35	0.40	0.02
CCSM4	0.47	0.38	0.49	0.05
SP-CCSM4	0.45	0.35	0.45	0.07
CESM1(BGC)	0.47	0.43	0.49	0.03
CESM1(CAM5)	0.45	0.47	0.40	0.05
CESM1(WACCM)	0.43	0.37	0.48	0.06
CMCC-CESM	0.34	0.26	0.52	0.13
CMCC-CM	0.41	0.40	0.43	0.10
CMCC-CMS	0.41	0.50	0.43	0.06
CNRM-CM5	0.50	0.60	0.43	0.07
CSIRO-Mk3.6.0	0.29	0.21	0.38	0.08
FGOALS-g2	0.46	0.40	0.58	0.15
GFDL-CM3	0.44	0.30	0.50	0.11
GFDL-ESM2G	0.31	–	0.30	0.15
GFDL-ESM2M	0.30	–	0.35	0.13
GISS-E2-H	0.31	0.30	0.28	0.03
GISS-E2-R	0.23	–	0.24	0.04
INM-CM4	0.45	–	0.42	0.12
IPSL-CM5A-LR	0.25	0.21	0.19	0.04
IPSL-CM5A-MR	0.19	0.16	0.17	0.07
IPSL-CM5B-LR	0.23	0.13	0.14	0.07
MIROC-ESM	0.62	0.71	0.45	0.14
MIROC-ESM-CHEM	0.62	0.79	0.52	0.11
MIROC4h*	–	–	–	–
MIROC5	0.47	0.31	0.62	0.13
MPI-ESM-LR	0.36	0.21	0.35	0.09
MPI-ESM-MR	0.39	0.41	0.48	0.09
MRI-CGCM3	0.44	0.24	0.58	0.15
NorESM1-M	0.39	0.40	0.53	0.11
NorESM1-ME	0.43	0.17	0.36	0.12
Multi-model mean (STD):	0.40 (0.10)	0.37 (0.17)	0.42 (0.12)	0.09

Table 2.1: Model-mean century-scale SAF from 2006-2099 and decadal-scale SAF from 2006-2028 and 2075-2097 using the CAM5 all-sky kernel. The final column shows models' internal variability in 21st century SAF via their standard deviation of 21st century mean 23-year SAF. Bold font highlights models showing significant SAF increases from 2006-2028 to 2075-2097. Asterisks denote models with historical data (included in Figure 1) but without 21st century data. Other "–" denote models that have no simulations with more than 0.5K temperature change over the respective time period.

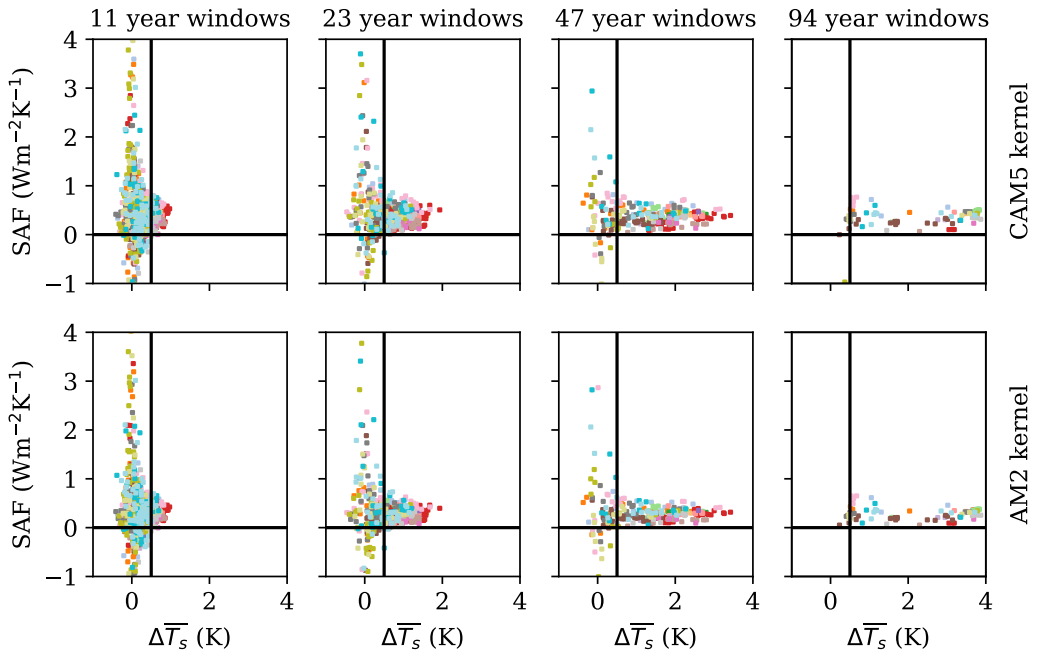

Figure 2.1: Surface albedo feedback (SAF) vs. change in global mean surface temperature ($\Delta\overline{T_s}$). SAF and $\Delta\overline{T_s}$ are derived from the CMIP5 multi-model ensemble of simulations across 11, 23, 47, and 94-year windows (by column) within historical and RCP8.5 experiments. Results are displayed for two all-sky radiative kernels (by row). Different colors represent different models and conform to those assigned by the key in Figure 2. Black lines bound data selected for further analysis ($\Delta\overline{T_s} > 0.5$ K & SAF $> 0\text{Wm}^{-2}\text{K}^{-1}$).

We hereafter use the 0.5K temperature change threshold as a cutoff to remove noisy SAF calculations and restrict the following analysis to only meaningful SAF in climate change. Use of different radiative kernels generally results in different scaling of the global SAF but does not result in significant relative changes between different models. Because the primary focus of this study is on the temporal variability of SAF across the CMIP5 models, we hereafter present results using primarily the CAM5 radiative kernel. Narrowing the remaining analysis to just one kernel minimally impacts our main findings while also reducing the study's dimensionality. Furthermore, because the following results are mostly independent of window length, we present our findings from only 23-year and 94-year calculations.

Similar to the considerable spread in the strength of snow albedo feedback reported by *Qu and Hall* (2014), the strength of SAF in the CMIP5 models is also highly variable, ranging from 0.1 to 0.8 $\mathrm{Wm^{-2}K^{-1}}$. Figure 2 shows the decadal-scale (23-year) temporal evolution of model- and multi-model mean (black) SAF using the CAM5 radiative kernel spanning three centuries. The temporal evolution of the multi-model mean decadal-scale SAF is dynamic, beginning above 0.7 in historical simulations, settling around 0.4 in the 21st century, and finally decreasing to below 0.1 $\mathrm{Wm^{-2}K^{-1}}$ after 2200. In the 21st century, multi-model mean SAF increases from 0.37 to 0.42 $\mathrm{Wm^{-2}K^{-1}}$. Using the AM2 radiative kernel yields lower values, where 21st century SAF increases from 0.27 to 0.33 $\mathrm{Wm^{-2}K^{-1}}$. SAF calculated from the CAM5 kernel is generally higher than when calculated from the AM2 kernel. This is likely due to improved cloud properties in the CAM5 resulting in reduced cloud masking over the Arctic (*Kay et al.*, 2012). Century-scale SAF calculated from the AM2 kernel in the 21st century is nearly identical to estimates reported by *Vial et al.* (2013) (0.3 $\mathrm{Wm^{-2}K^{-1}}$) in four times CO_2 experiments. Results from historical simulations are few after applying the 0.5K temperature change cutoff, while simulations extending beyond 2100 are fewer altogether in the CMIP5 multi-model ensemble dataset. In

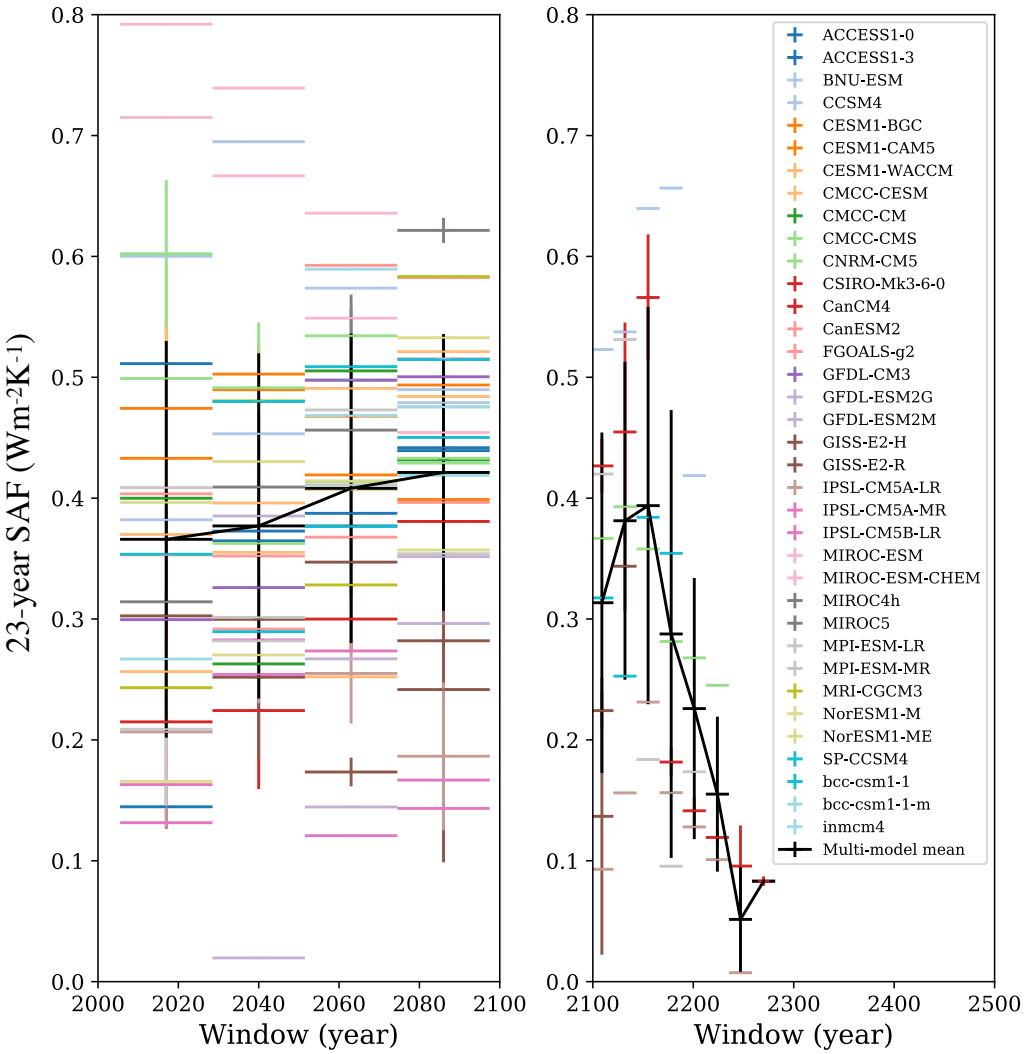

Figure 2.2: Temporal evolution of surface albedo feedback (SAF) in CMIP5 models calculated using the CESM1-CAM5 radiative kernel. Horizontal line segments mark 23-year ensemble mean SAFs in individual models (colors) calculated from multiple ensemble members. Black (connected) horizontal line segments mark multi-model mean 23-year SAF. Vertical error bars on individual model means represent ensemble member standard deviations. Black vertical error bars on multi-model means represent model standard deviations. Data displayed are calculated only from 23-year periods with at least 0.5 K global mean surface temperature change.

these extended simulations, multi-model mean SAF decreases monotonically after 2150, decreasing from just under 0.4 to below 0.1 $Wm^{-2}K^{-1}$ by 2250.

The relatively large multi-model variability obscures the small but statistically significant (p-value = 0.04) increase in 21st century model-mean decadal-scale SAF. Using the 2006-2028 and 2075-2097 values from Table 1, where we show each model's mean early and late 21st-century decadal-scale SAF, respectively, we apply a paired difference test to determine the significance of this apparent increase. The results reveal a statistically significant increase in the models' mean 21st century decadal-scale SAF of 0.07 $Wm^{-2}K^{-1}$, about the same as the 0.06 $Wm^{-2}K^{-1}$ increase in the multi-model mean SAF over the same period. Because of the relatively large statistical uncertainty (+/- 0.06 $Wm^{-2}K^{-1}$; 95% C.I.), however, we must only interpret these results as positive but small change and most likely not negative change in 21st century SAF.

Finally, we regress each model's 21st century (94-year) ensemble-mean SAF, shown in Table 1 (2006-2099) against its corresponding 21st-century mean decadal-scale (23-year) SAF in Figure 3 (left). Encouragingly, model-mean 21st century 94-year SAF is strongly correlated ($r^2 = 0.90$) with 21st century model-mean 23-year SAF. This strong correlation (standard error of regression = 0.05 $Wm^{-2}K^{-1}$) demonstrates that in general, 23-year SAF calculations are well representative of their century time-scale SAF. When we regress 23-year SAFs from only the first 23-year window (2006-2028) onto the 94-year SAFs (Figure 3, right), however, the correlation weakens ($r^2 = 0.65$). The weaker correlation (standard error of regression = 0.07 $Wm^{-2}K^{-1}$) indicates that 23-year estimates of SAF from any one period are not strong predictors of century-scale SAF in transient climate. This finding is somewhat intuitive, as a single 23-year estimate of SAF cannot predict how SAF will evolve in a changing climate. Because 21st century mean 23-year SAF is strongly correlated with 21st century 94-year SAF, however, 23-year estimates of SAF can accurately quantify sub-century scale SAF

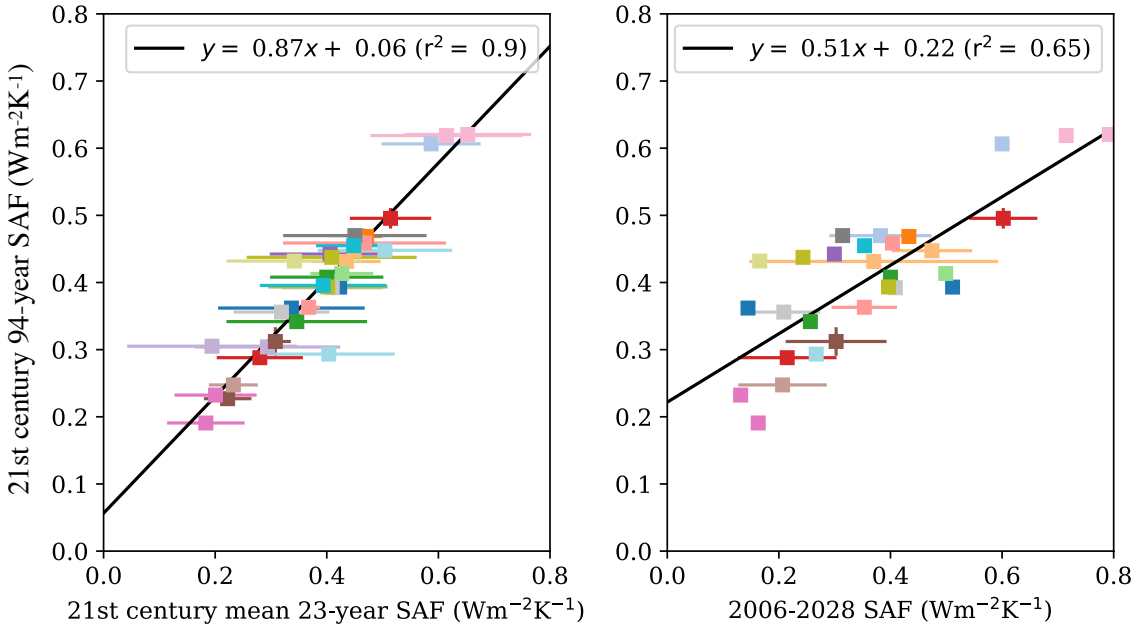

Figure 2.3: 21st century 94-year model mean SAFs vs. 21st century 23-year model mean SAFs. Scattered data are displayed with their linear regressions plotted in black. On the left, 23-year model means are calculated from all four 23-year windows within the 21st century. Horizontal error bars represent standard error of ensemble member 23-year means. On the right, 23-year means are calculated from ensemble members with only the 2006-2028 period. Horizontal error bars represent ensemble member standard deviations. As in Figure 2, data displayed are calculated only from periods with at least 0.5 K global mean surface temperature change. Colors are assigned by model accordingly to the key in Figure 2.

as long as there is at least 0.5K temperature change. This is useful for examination of the temporal variability within a longer timescale. These findings justify using 23-year SAF to quantify time evolving decadal-scale SAF, but using a temporally limited dataset to derive accurate estimates of long-term SAF in climate change is subject to considerable uncertainty.

With multiple decadal-scale SAF estimates in 21st century climate simulations, we conclude that SAF does not decrease about its multi-model mean of 0.4 (+/- 0.1) $Wm^{-2}K^{-1}$ and possibly strengthens throughout the 21st century. Of the 29 models with both early (2006-2028) and late (2075-2097) 21st century 23-year SAF in Table 1, 16 (55%) show significant strengthening of SAF. With most CMIP5 models showing significant strengthening in SAF, multi-model mean SAF increasing, and a significant increase from the paired difference test, the CMIP5 multi-model ensemble results suggest SAF does not weaken in the 21st century. This finding is contrary to our initial expectations in simulations where diminishing Arctic sea-ice is common. Further investigation into the spatial distribution of the changing TOA net irradiance reveals more rapid Arctic albedo decline in late spring and early summer months toward the end of the 21st century. Figure 4 gives a glimpse into this more rapid Arctic albedo decline in June, where we show the 23-year change in TOA net irradiance in the early versus late 21st century in the CanESM2 and CESM1(WACCM) models. We select simulations from these two models because they have increasing 21st century SAF, relatively small 23-year standard deviations, and values similar to multi-model means in Table 1. In both simulations, June Arctic albedo decreases more rapidly in the late versus early 21st century. The increasing Arctic albedo decline is typical among other models as well, suggesting that sea-ice decline is a key driver of persistent SAF strength throughout the 21st century. Increasing Antarctic albedo decline is also evident in Southern Hemisphere summer months.

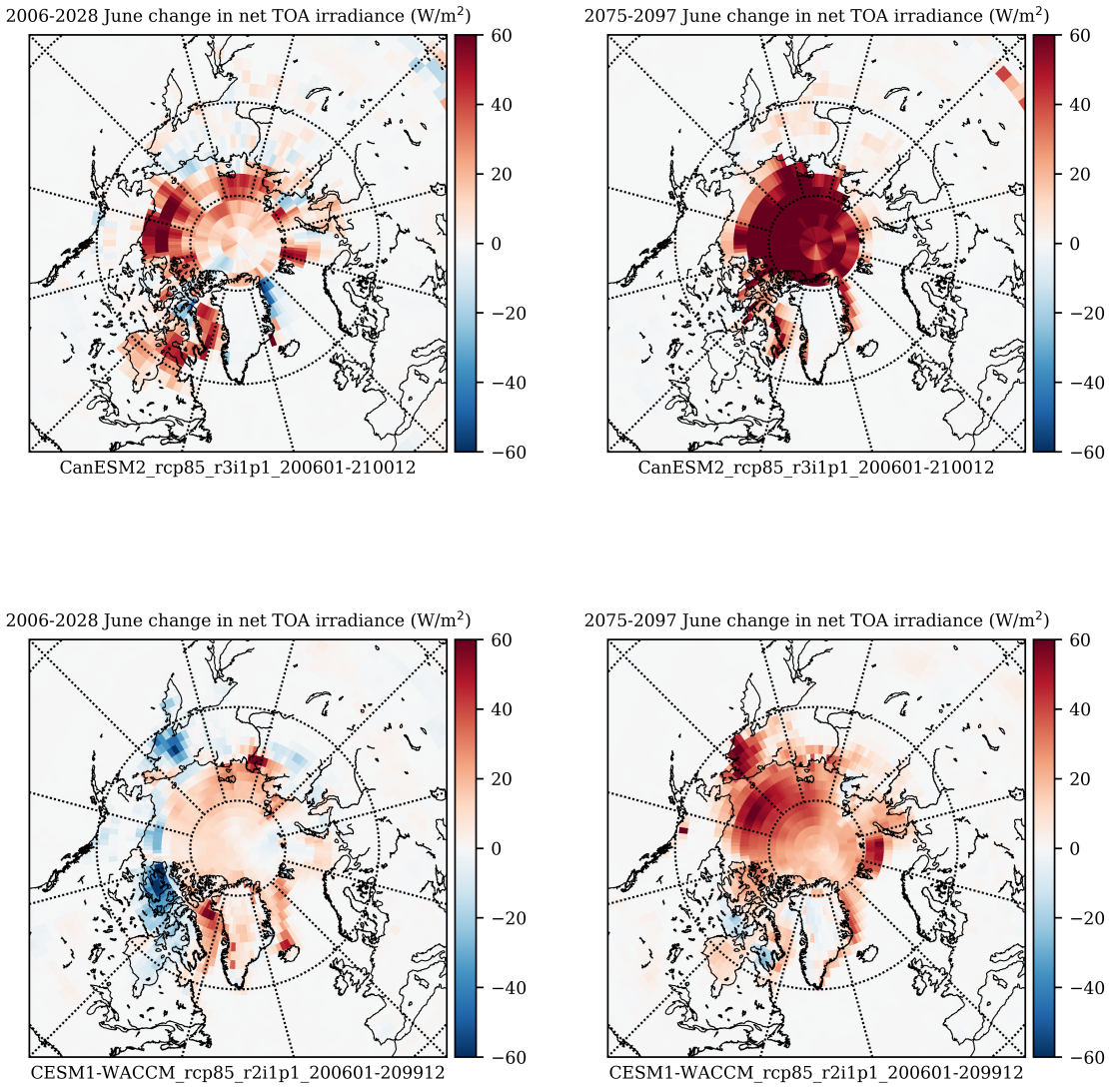

Figure 2.4: June 23-year change in net TOA irradiance caused by surface albedo changes in the early (left) versus late (right) 21st century. Filled contours map results from single ensemble member simulations in CanESM2 (top) and CESM1-WACCM (bottom) for northern latitudes (> 45 degrees N). Positive (red) values indicate increasing net TOA irradiance from decreasing surface albedo.

2.4 Conclusions

This study examined decadal-scale variability of SAF using 36 climate models in the CMIP5 multi-model ensemble archive. After identifying asymptotic behavior in its calculation, we removed noisy SAF contributions by selecting only estimates from time periods exhibiting global mean temperature change of at least 0.5K for analysis. This allowed for better interpretation of model and multi-model mean statistics from which we identified a relatively small but significant (p-value = 0.04) 18% increase (+/- 16%; 95% confidence interval) in SAF strength from 2017 to 2086. We regressed century-scale against decadal-scale SAF and verified that multiple shorter time-scale estimates are good predictors of their longer time-scale counterparts, while single 23-year estimates have limited utility. Finally, we investigated the spatial distribution of the changing TOA net irradiance and determined that late spring to early summer Arctic albedo declined more rapidly in late versus early 21st century years in most models. We found evidence of dominant sea-ice contribution to persistent SAF strength late into 21st century simulations.

The main implications of these findings follow. First, that decadal-scale SAF is correlated with century-scale SAF provides justification for using decadal-scale estimates to evaluate time-dependent variability of SAF. Extending SAF derived from remote sensing observations, (e.g., *Flanner et al.* (2011), *Pistone et al.* (2014), *Cao et al.* (2015)) that are limited in their temporal domain by the satellite era, onto longer time scales, however, is feasible but with limited accuracy. These results are of course restricted to time periods with sufficient climate change (> 0.5 K), and also predicated on model behavior exhibiting similar multi-decadal characteristics as the real climate system. Second, that CMIP5 multi-model ensemble mean SAF increases in the 21st century despite rapid seasonal snow and sea-ice cover loss demonstrates a persistent capacity for global surface albedo change extending through the end of the century. A closer look at the spatial distribution of albedo trends revealed a poleward

shift in maximal albedo decline as well as late-spring to early summer prevalence in Arctic and Antarctic sea-ice melt.

CHAPTER III

Measuring Snow Specific Surface Area with 1.30 and 1.55μm Bidirectional Reflectance Factors

Abstract:

Snow specific surface area (SSA) is an important physical property that directly affects solar absorption of snow cover. Previous instrumentation to measure snow SSA is commercially available for purchase, but these instruments are costly and / or remove and destroy snow samples during data collection. To obtain rapid, repeatable, and in situ surface snow SSA measurements, we mounted infrared light emitting- and photo-diodes into a 17cm diameter black styrene dome. By flashing light emitting diodes and measuring photodiode currents, we obtain accurate 1.30 and 1.55μm bidirectional reflectance factors (BRFs). We compare measured snow BRFs with X-ray micro-computed tomography scans and Monte Carlo photon modeling to approximate snow SSA. These comparisons show an exponential relationship between snow 1.30μm BRFs and SSA from which we calculate calibration functions to approximate snow SSA. Mapping measured snow 1.30μm BRFs to SSA enables rapid retrieval of snow SSA by a new instrument called the Near-Infrared Emitting and Reflectance-Monitoring Dome.

3.1 Introduction

Earth's surface albedo is a primary component of the planetary energy budget. Of the vast natural surface types that determine Earth's fundamental radiative properties, snow cover is the most reflective. Fresh snow cover is especially reflective in the visible and less so in the near-infrared spectra, reflecting as much as 90 percent of the direct solar irradiance into the upward facing hemisphere. Snow cover is also a highly dynamic, unstable surface type in the Earth system. Changes in snow albedo, for example, drive positive albedo feedback and other nonlinear processes that can enhance snow melt and surface temperature anomalies (*Fletcher et al.*, 2012; *Qu and Hall*, 2007; *Winton*, 2006a; *Hall*, 2004). Positive snow internal albedo feedback occurs due to the strong dependence of snow infrared reflectance on snow specific surface area (SSA). The Snow, Ice, and Aerosol Radiation (SNICAR) model (*Flanner et al.*, 2007) demonstrates this dependence and is applied here to simulate the spectral black-sky albedo of nadir illuminated snow in Figure 1.

Snow SSA is defined as the total ice surface area to mass ratio, such that

$$\text{SSA} = S/M = \frac{S}{\rho_{ice} V}, \tag{3.1}$$

where S is the total surface area of a mass M of snow particles occupying an ice volume V and ρ_{ice} is the density of ice (917 kg/m^3) (*Legagneux et al.*, 2002; *Gallet et al.*, 2009). *Domine et al.* (2006) and *Gallet et al.* (2009) demonstrate the strong dependence of snow infrared reflectance on snow SSA. Modeling studies, such as *Wiscombe and Warren* (1980) and *Flanner et al.* (2007), also demonstrate this strong dependence using sphere effective radius as an optical metric for snow grain size. *Gallet et al.* (2009) also quantify snow SSA by its sphere effective radius (r_{eff}), defined by the radius of a sphere having the same surface area to volume ratio as the particles, such

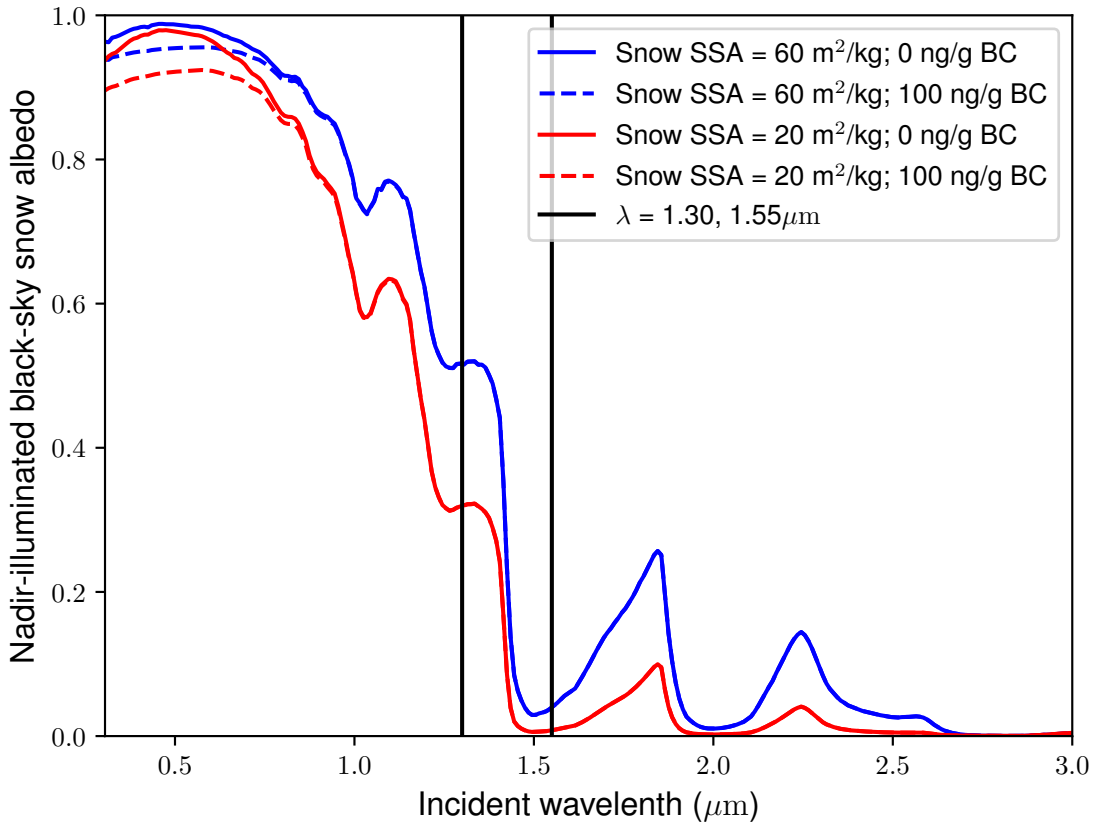

Figure 3.1: Black-sky spectral snow albedo under nadir illumination simulated using the Snow, Ice, and Aerosol Radiation (SNICAR) model (*Flanner et al.*, 2007). Solid curves represent clean snow of medium-high SSA ($60 m^2/kg$, blue) and medium-low SSA ($20 m^2/kg$, red) to show the dependence of snow albedo on snow SSA. Dashed lines represent contaminated snow with uncoated black carbon (BC) particulate concentrations of 100 ng/g. 100 ng/g of BC in snow directly reduces visible but not infrared albedo. The dependence of snow albedo on SSA but not on BC concentration at 1.30 and 1.55μm motivates the use of these wavelengths for measurement of snow grain size.

that

$$\mathrm{SSA} = \frac{3}{\rho_{ice} r_{eff}}. \tag{3.2}$$

Other studies (e.g., *Jin et al.* (2008)) quantify snow grain size by its sphere effective

radius (RE) as it relates to the projected area of a particle, so that

$$\mathrm{RE} = \frac{3}{4}(V/A), \tag{3.3}$$

where A is the particle projected area. These expressions of sphere effective radii, r_{eff} and RE, defined by ice particle surface area S versus ice particle projected area A, respectively, are equivalent for convex bodies (see Appendix B).

As surface temperatures increase, snow albedo generally decreases as snow SSA decreases. Recent studies verify this process of natural snow metamorphosis on seasonal timescales in Antarctica (*Libois et al.*, 2015), New Hampshire (*Adolph et al.*, 2017), and Colorado (*Skiles and Painter*, 2017). *Libois et al.* (2015) observe relatively slow SSA evolution in the extremely cold Antarctic environment. *Adolph et al.* (2017) monitor the evolution of snow albedo across three winter seasons in New Hampshire and discover a strong dependence of snow broad-band albedo on optically derived snow grain size (r_{eff}). These observational studies inform us on snow albedo measurements conducted on clean snow, with small concentrations of light absorbing impurities (LAI) such as dust and black carbon (BC). *Skiles and Painter* (2017) also observe seasonal scale snow albedo decline in springtime Colorado. In contrast, however, they find that snow albedo is primarily related to dust concentration. LAI can directly reduce snow albedo, but also indirectly darkens snow during metamorphosis. *Hadley and Kirchstetter* (2012), for example, demonstrates that the albedo reduction due to the presence of BC in snow is amplified in snow of lower SSA. This enhancement of snow albedo reduction is another source of instability in the snow pack that increases the strength of snow internal albedo feedback.

When snow SSA decreases, a positive albedo feedback exists where solar heating induces grain growth, further decreases SSA, and causes the snow surface to absorb additional solar radiation. Surface warming can reduce snow grain growth

rates, however, if growth processes from vapor diffusion and strong temperature gradients are affected negatively (*Flanner and Zender*, 2006). Recent studies use X-ray computed microtomography (X-CT) to monitor the evolution of snow SSA in a high-temperature gradient (*Wang and Baker*, 2014) and in isothermal snow metamorphosis (*Ebner et al.*, 2015). In *Ebner et al.* (2015), measurements of snow SSA evolution in isothermal snow agree with the isothermal snow metamorphosis modeling framework developed by *Legagneux et al.* (2004) and *Legagneux and Domine* (2005). These studies express snow SSA in isothermal metamorphosis as function of time t as follows,

$$\mathrm{SSA} = \mathrm{SSA}_0 \left(\frac{\tau}{\tau + t} \right)^{1/n}, \tag{3.4}$$

for initial snow SSA_0 at $t = 0$ and adjustable parameters τ and n.

Previous studies establish techniques to accurately obtain snow SSA using methane gas absorption (*Legagneux et al.*, 2002), contact spectroscopy (*Painter et al.*, 2007), infrared hemispherical reflectance (*Gallet et al.*, 2009; *Picard et al.*, 2009; *Gallet et al.*, 2014; *Gergely et al.*, 2014), and X-CT in cold rooms (*Pinzer and Schneebeli*, 2009; *Wang and Baker*, 2014; *Ebner et al.*, 2015), but these methods require expensive, heavy equipment and measurements can be time consuming. Further, previous methods require that snow samples are collected and possibly even destroyed during measurements, preventing in situ snow observations over the span of just several hours. Because of the strong dependence of snow albedo on snow SSA (*Adolph et al.*, 2017), the ability to obtain rapid, repeatable measurements that can describe the snow surface in basic physical terms is widely sought after.

Here, we introduce a new technique to measure snow-SSA in a non-destructive manner using 1.30 and 1.55 μm directional reflectance. By gently placing the Near-Infrared Emitting and Reflectance-monitoring Dome (NERD) onto the snow surface, multiple 1.30 and 1.55μm bidirectional reflectance factors (BRFs) are obtained in just

minutes with minimal alteration of the snow surface. To calibrate with respect to snow SSA, we compare snow BRFs with X-CT derived SSA to identify the exponential relationship between SSA and snow 1.30μm BRFs.

3.2 Instrumentation and Methods

3.2.1 The Near-Infrared Emitting and Reflectance-Monitoring Dome

The NERD is designed to measure 1.30 and 1.55 μm BRFs. Four light emitting diodes (LEDs) and four photodiodes are mounted into a 17cm black styrene half-sphere (see Figure 2). Two LEDs with peak emission wavelengths of 1.30μm are mounted at nadir and 10 degrees relative to zenith while two LEDs with peak emission wavelengths of 1.55μm are mounted at 15 degrees off nadir. 1.30μm LEDs have spectral line half widths of 85nm and half intensity beam angles of 10 degrees, while 1.55μm LEDs have half-maximum bandwidths of 130nm and 20 degree beam angles. These high-powered infrared LEDs are selected to illuminate a small oval of the experimental surface to maximize the reflected radiance signal. The reflected radiance signal is measured using four InGaAs photodiodes mounted in two different azimuthal planes; two each at 30 and 60 degrees relative to zenith. Photodiodes highly sensitive to light ranging from 800 to 1750nm and relatively large active areas (1mm) are selected to maximize sensitivity.

The NERD is similar to that of the DUal Frequency Integrating Sphere for Snow SSA measurements (DUFISSS) (*Gallet et al.*, 2009) in that it uses 1.30 (1.31 in DUFISSS) and 1.55 μm emitters to illuminate the snow surface from nadir (15 degrees off nadir for 1.55 μm in NERD). LEDs are toggled using a Ruggeduino-ET (Extended temperature, operational down to -40 degrees C.; https://www.rugged-circuits.com/microcontroller-boards/ruggeduino-et-extended-temperature-40c-85c) connected to a LED driver. The LED driver drives an 80mA square wave through each

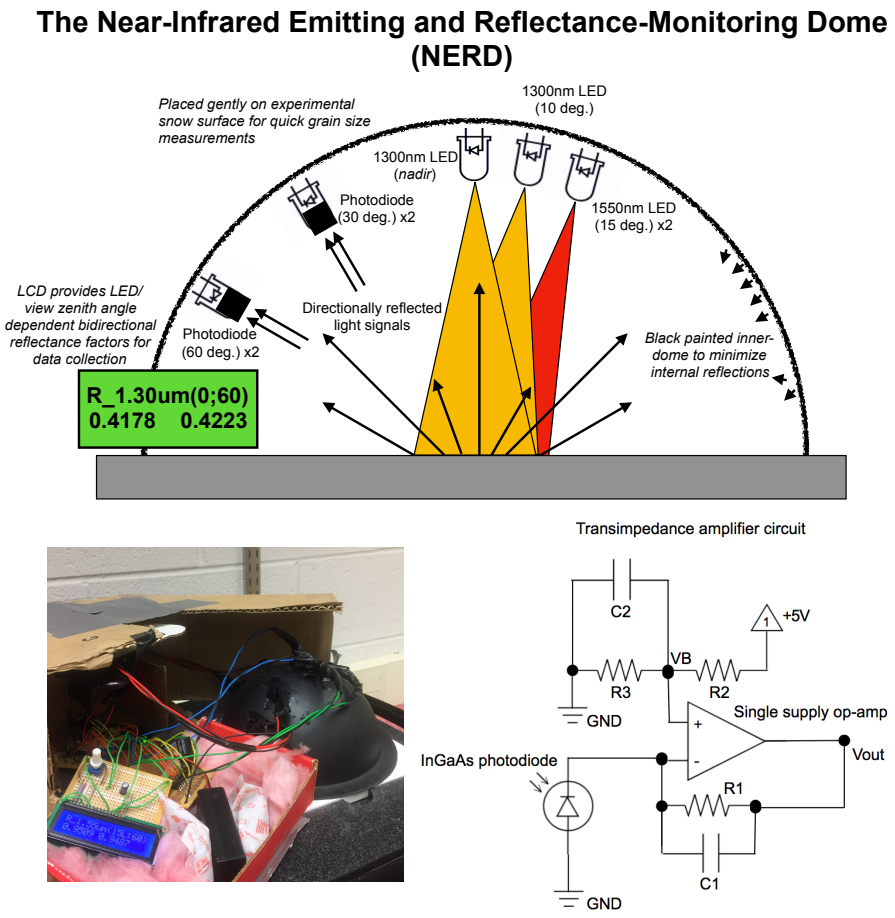

Figure 3.2: Near-Infrared Emitting and Reflectance-Monitoring Dome (NERD) schematic, photograph, and transimpedance amplifier circuit diagram. Two instruments are engineered with different photodiode responsivities. Photodiode responsivities are determined by the feedback resistance (R1) in the transimpedance amplifier circuits. Using feedback resistances of as low as four mega-Ohms in a low responsivity NERD and as high as fifteen mega-Ohms in a high responsivity NERD yield dynamic reflectance factor responses over the range of 0 to 0.95 at 1.30 and 1.55µm.

LED individually with a pulse width of two seconds (20% duty cycle). The main distinction between the DUFISSS and the NERD is the type of reflectance measured. *Gallet et al.* (2009) use an integrating sphere to measure hemispherical reflectance. Here, rather, we direct photodiodes toward the illuminated surface in a black dome to measure BRFs. The interior of the dome is painted with a flat black paint to increase absorptivity and minimize internal reflections between the dome and snow

surface. To detect reflected radiance signals, photodiodes are reverse biased to induce currents linearly related to the amount of light incident on its active region. Because these light signals are reflected from the experimental surface, the currents induced by the photodiodes are very small (nano- to micro-Amps). To measure the small currents, the photodiodes are connected to transimpedance amplifiers (as in Figure 2). The transimpedance amplifier circuits convert and amplify the small photodiode currents into measurable voltage signals. Finally, an active low pass filter is installed between the amplifier and the analog-to-digital converter (ADC) and reduces noise. This filter is designed to have a time constant of less than 0.5 seconds to achieve balance between adequate noise reduction and speed. Waiting 0.75 seconds after toggling the LED allows for enough time for the photodiode current to stabilize. After these currents stabilize, 100 voltage samples (ranging from 0.1 to 1.0 Volts) are then rapidly collected using the Ruggeduino-ET's ADCs. Average voltage obtained during active illumination is differenced from average dark current voltage output to derive reflectance factors. Because the orientation of LEDs and photodiodes are fixed, reflectance factors can be obtained after calibration using two diffuse reflectance targets in a manner similar to that used by *Gallet et al.* (2009), *Gergely et al.* (2014), and *Dumont et al.* (2010). These Lambertian targets reflect incident light according to Lambert's cosine law and appear equally bright at all viewing angles. The reflectance of the targets are measured with high precision across a broad spectrum. At 1.30 (1.55) μm, the white and gray targets have calibrated reflectances of 0.95073 (0.94426) and 0.42170 (0.41343), respectively, as reported by the manufacturer. By comparing the measured voltage signal from the experimental (snow) surface to that measured from the reflectance targets, two BRFs at both 30 and 60 degree viewing angles are obtained for each light source. This procedure enables simultaneous measurements of multiple BRFs at 1.30 and 1.55 μm.

To validate NERD reflectance measurements, we assess its measurement accu-

Table 3.1: NERD Lambertian Reflectance Measurements

$\lambda = 1.30\mu$m		Median BRF (RMS error)			
n	ρ_L	$R(0°; 30°)$	$R(0°; 60°)$	$R(10°; 30°)$	$R(10°; 60°)$
10	0.422	0.399 (0.021)	0.422 (0.016)	0.415 (0.015)	0.434 (0.015)
10	0.951	0.939 (0.013)	0.944 (0.015)	0.958 (0.018)	0.952 (0.010)
N		Linear regression; $\hat{R}(\rho_L) = A\rho_L + B$			
20	$\hat{R} =$	{1.023ρ_L - 0.028,	0.987ρ_L + 0.007,	1.031ρ_L - 0.024,	0.980ρ_L - 0.018}
$\lambda = 1.55\mu$m		Median BRF (RMS error)			
n	ρ_L	$R(15^\circ_a; 30°)$	$R(15^\circ_a; 60°)$	$R(15^\circ_b; 30°)$	$R(15^\circ_b; 60°)$
10	0.413	0.410 (0.009)	0.420 (0.017)	0.411 (0.008)	0.420 (0.021)
6	0.944	0.959 (0.012)	0.963 (0.019)	0.960 (0.013)	0.964 (0.020)
N		Linear regression; $\hat{R}(\rho_L) = A\rho_L + B$			
16	$\hat{R} =$	{1.028ρ_L - 0.016,	1.016ρ_L + 0.003,	1.026ρ_L - 0.014,	1.011ρ_L + 0.009}

racy, precision, and responsivity by measuring BRFs of reflectance standards after calibration. Using both reflectance standards, we record ten BRF (R) measurements for each LED / photodiode viewing zenith angle ($\theta_i; \theta_r$) combination during outdoor temperatures between -20° and +2° Celsius (C.). In general, NERD BRFs of the Lambertian reflectance standards are accurate to within +/- 2%. We quantify instrument precision (2%) by computing root mean squared (RMS) errors from repeated measurements (see Table 1). Linear regressions quantify the linear responsivity (A) over the reflectance range of 0.41 to 0.95. Responsivity error ranges from -2% to +3% and from +1% to +3% at 1.30 and 1.55 μm, respectively. These results validate the NERD's ability to obtain precise BRFs with a measurement uncertainty of 1-2%.

3.2.2 X-ray Microcomputed Tomography

Snow BRFs measured by the NERD are complemented by X-CT scans. X-CT scans of snow are conducted at the U.S. Army's Cold Regions Research Engineering Laboratory (CRREL) in Hanover, New Hampshire. The machine is housed in a cold lab kept below 0°C. allowing for X-CT of snow without significant melt.

Small samples of snow are collected in roughly 10cm tall cylindrical plastic sample holders and placed into the machine. An X-ray source is emitted at 40-45kV and 177-200 micro-Amps. X-ray transmittance is measured as the machine rotates the sample. Setting the exposure time to 340ms at a pixel resolution of 14.9μm with rotation steps at 0.3-0.4 degrees allow for fast scan times of roughly 15 minutes. These short scan times are necessary to complete the scan without too much absorbed radiation melting the snow. Processing software allows for samples to be reconstructed while computing physical properties of which SSA are derived (*Pinzer and Schneebeli*, 2009). 3-dimensional visualization software is used to generate images shown in Figure 3.

3.2.3 Snow Samples

Snow samples for NERD snow SSA calibration were collected over the span of three years (winters 2015-2017). Measurements of these samples were conducted during the months of February and March in 2016 and 2017 in Hanover, New Hampshire.

3.2.3.1 Fresh samples from 2016

Fresh snow samples were collected during a late winter snow fall event in 2016 just outside of Hanover, New Hampshire. Fresh snow from two different locations were scooped into coolers and then transported to the CRREL for analysis. Visual inspection of these samples revealed snow that appeared softer and less dense than the class of old samples. Because the surface temperature was close to 0°C., the samples appeared to be wet. X-CT scans (Figure 3a.) confirmed snow that was of relatively medium density (350 kg/m^3), medium porosity (62%), and medium SSA (19 m^2/kg).

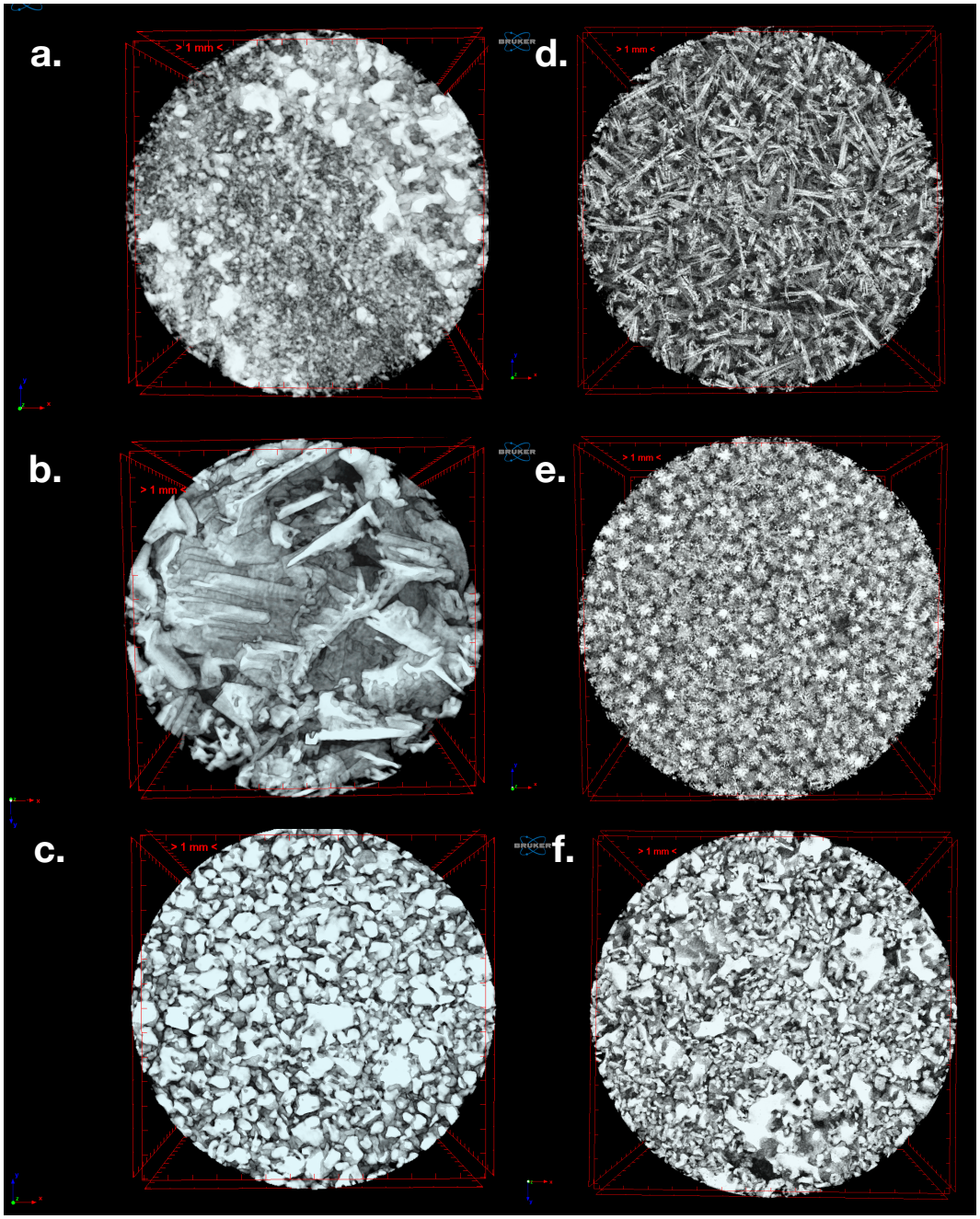

Figure 3.3: X-ray microcomputed tomography (X-CT) images of snow samples (15mm diameter) collected across three winters (2015-2017) in Hanover, New Hampshire. Snow samples shown on the left (a., b., c.) were scanned during 2016, while those on the right (d., e., f.) were scanned in 2017. Generally (except for b.), snow specific surface area, derived from X-CT analysis software, decreases as snow grains appear more rounded.

3.2.3.2 Artificial ice crystals grown in a cold lab

One of the snow samples included in the NERD snow SSA calibration was grown inside a cold lab at -20° C. using a forced temperature gradient. Analysis on this sample was conducted during winter of 2016. Visual inspection revealed a hardened ice medium with a well defined crystalline structure. X-CT scans (Figure 3b.) showed jagged ice micro-features of relatively medium density (320 kg/m^3), medium porosity (65%), and low SSA (9 m^2/kg).

3.2.3.3 Old sintered samples from 2015

The oldest class of snow samples used for the NERD calibration were collected during the 2015 winter season in Hanover, New Hampshire. These samples were then stored in a cold laboratory for a year at the CRREL at approximately -20° C. During February of 2016, visual inspection revealed snow that was highly sintered. As expected, X-CT scans (Figure 3c.) confirmed that these two samples, distinguishable only by the container they were stored in, were of relatively high density (610 kg/m^3), low porosity (33%), and low SSA (9 m^2/kg).

3.2.3.4 Fresh needles collected during the March 14 snow storm

On March 14, 2017, a heavy daytime snow fall event in Hanover, New Hampshire enabled rapid collection and analysis of snow samples. Cylindrical X-CT sample containers were placed in snow already on the ground. Snow fall filled sample containers in just a couple hours. Sample containers were carefully moved (with gloves) into coolers. Coolers were then rushed directly into the nearby lab for X-CT analysis. X-CT scans (Figure 3d.) confirmed needle like ice structures. These structures presented a snow pack of relatively low density (110 kg/m^3), high porosity (88%), and high SSA (66 m^2/kg).

3.2.3.5 Fresh samples collected shortly after February (10-16) 2017 snow fall events

Moderately fresh snow samples were collected in the first couple days following snow storms in February 2017 in Hanover, New Hampshire. A few of these samples include snow with small amounts of added dust and BC. All samples with added LAI included in the NERD SSA calibration dataset were first screened to remove samples with heavy LAI loads that caused direct snow darkening at 1.30 and 1.55 μm. Snow samples were shoveled into coolers and transported to the CRREL for X-CT analysis. X-CT scans (Figure 3e.) revealed snow of relatively low density (170 kg/m^3), high porosity (82%) and medium-high SSA (54 m^2/kg).

3.2.3.6 Samples collected after apparent metamorphosis on February 17 2017

After visibly apparent snow metamorphosis, partially aged snow from Hanover, New Hampshire was collected and transported to the CRREL for X-CT analysis. Some of these samples include snow with added LAI. Samples with added LAI had shown visible signs of dramatic metamorphosis. X-CT scans (Figure 3f.) confirmed these observations, revealing snow of relatively medium density (310 kg/m^3), medium porosity (66 %), and medium SSA (23 m^2/kg).

3.2.4 Monte Carlo Modeling of Bidirectional Reflectance Factors

The Monte Carlo method for photon transport is used to model three-dimensional light scattering within a snow pack. NERD LEDs are modeled as photon emitters according to their placement within the dome. An array of photons with wavelengths generated at random using a Gaussian distribution are used to mimic the 85 and 130nm full width at half-maximum spectral emission characteristics of the narrow-band LEDs. Photons are initiated downward into the snow medium as in *Kaempfer*

et al. (2007) and propagated in optical depth space. Photon particle interactions are determined using random number generators and can either be absorbed or scattered with the probability determined by the particle single scatter albedo. Photons are terminated upon absorption, but the overwhelmingly likely event is scattering because of the relatively high single scatter albedo of ice at these wavelengths. When the photon is scattered, its new direction cosines are determined by the specific particle scattering phase function.

To generate theoretical calibration curves mapping snow BRFs to snow SSA, we run multiple simulations for various particle SSA ranging from 10 to 90 m^2/kg. At least 10^5 photons per simulation are propagated and followed through the snow medium until they are absorbed or exit the medium. The snow medium is modeled as a homogenous matrix of suspended particles with input data containing the particle mass absorption cross section, asymmetry parameter, single scattering albedo, projected area, volume, and scattering matrix from *Yang et al.* (2013). Ice particle shape habits include spheres, droxtals, solid hexagonal columns, and solid hexagonal plates. We select these subset of shape habits from the larger dataset provided by *Yang et al.* (2013) because they are purely convex solid ice particles. Because they are convex bodies, their SSAs can be computed from the projected area and volume. To generate theoretical calibration curves mapping snow BRFs to snow SSA, we run multiple simulations for various particle SSA ranging from 10 to 90 m^2/kg.

Reflected light from Lambertian surfaces is simulated using the Monte Carlo model to test its statistical uncertainty. To this end, azimuthal-mean BRFs are calculated according to the reflectance definitions presented by *Dumont et al.* (2010); *Hudson et al.* (2006); *F.E. Nicodemus et al.* (1977). Accordingly, photon exit angles are grouped into 30 exit zenith angle (θ_r) bins at 3 degree resolution. Azimuthal-mean

BRFs are calculated by zenith angle θ_r from the total incident photon flux $d\Phi_i$ by

$$R(\theta_i;\theta_r) = \int_0^{2\pi} \frac{d\Phi_r}{2\sin\theta_r \cos\theta_r d\Phi_i} d\phi_r \tag{3.5}$$

where Φ_r represents the azimuthally integrated photon flux through each θ_r bin. In the denominator, the $\cos\theta_r$ factor satisfies Lambert's cosine law while $\sin\theta_r$ accounts for the zenith angular dependence of the azimuthally integrated projected solid angle. Finally, the factor 2 is necessary to normalize the resulting weighting function $w(\theta_r) = \sin\theta_r \cos\theta_r$, as

$$\int_0^{\pi/2} \sin\theta_r \cos\theta_r d\theta_r = \frac{1}{2}. \tag{3.6}$$

Equation (5) is applied to Monte Carlo simulations of 75,000 photons reflected by Lambertian surfaces having reflectances of 0 to 1. At 3-degree resolution, 30 and 60 degree BRFs of Lambertian surfaces are simulated accurately to within +/- 2%. Monte Carlo noise from 75,000 photons are quantified by computing RMS errors across the full range of Lambertian reflectances. Across this range, RMS errors at 30 and 60 degrees are generally less than 0.01. These relatively small RMS errors computed from just 75,000 simulated photons justify computing accurate BRFs at 3-degree resolution.

3.3 Results and Discussion

To examine the relationship between snow SSA and 1.30 and 1.55 μm BRFs, we compare X-CT derived snow SSA with NERD snow measurements. To this end, we conduct side-by-side X-CT and NERD analysis of all snow samples described in the preceding section. In general, NERD BRFs are directly related to snow SSA (Figure 4). At 1.30 μm, NERD snow BRFs are slightly higher at 60 degrees than at 30 degrees. Despite the direct relationships between NERD snow BRFs and X-CT derived snow

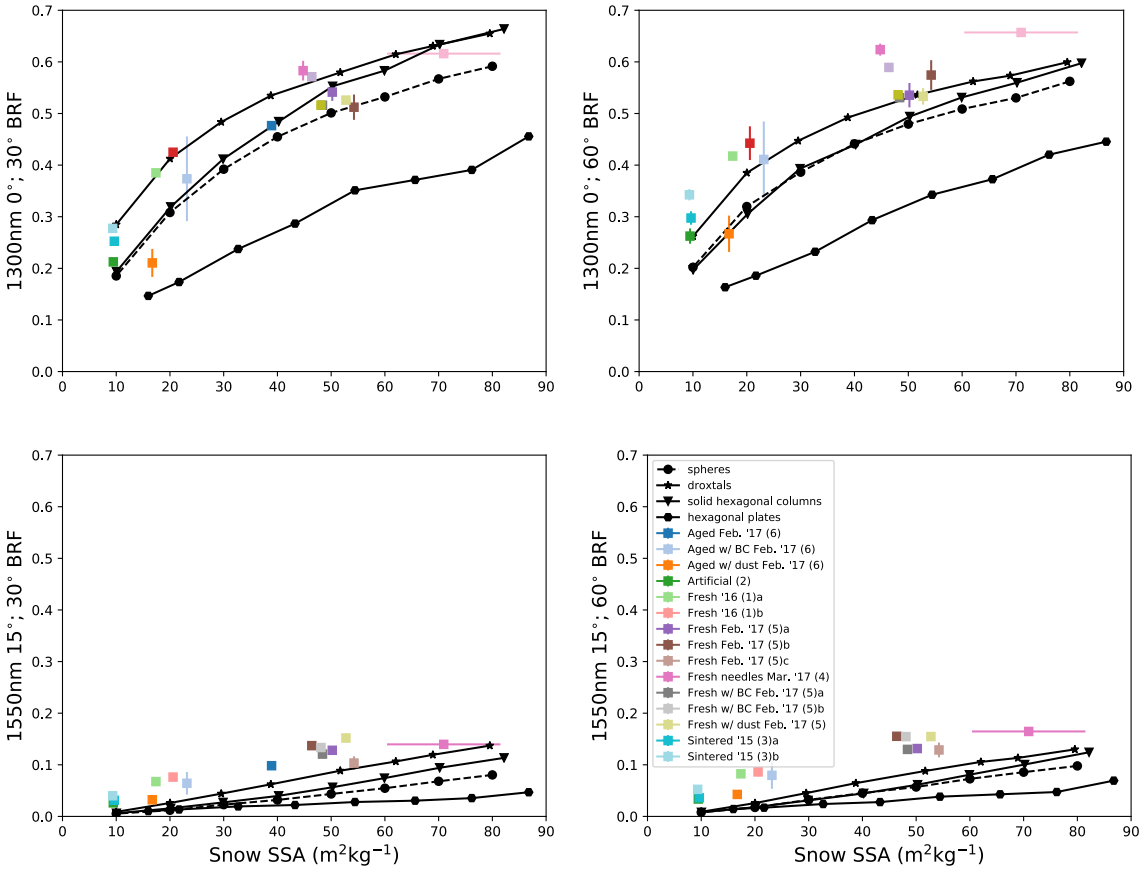

Figure 3.4: 1.30 (top) and 1.55 (bottom) μm 30 (left) and 60 (right) degree bidirectional reflectance factors (BRFs) versus snow specific surface area (SSA). Black line segments connect BRFs calculated from Monte Carlo simulations of photon pathways through snow mediums comprised of spheres (circles, dashed lines), droxtals (stars), solid hexagonal columns (triangles), and hexagonal plates (hexagons). Measured BRFs with the NERD are scattered against X-CT derived snow SSA (colored squares). Snow samples labeled in the key relate directly to those described in the previous section. Vertical error bars on NERD BRFs represent standard deviations calculated from multiple azimuthal samples. Horizontal error bars on X-CT derived SSA, where present, represent standard deviations from multiple scans on similar snow samples.

SSA, there exists considerable spread in measurements at both wavelengths and at both viewing angles. The spread in measurements results in considerable uncertainty in the ability to retrieve snow SSA from NERD BRFs. In the following subsections,

we discuss NERD reflectance measurement validation and results from Monte Carlo simulations in the context of previous studies. Finally, we synthesize our findings in a subsection that gives an analytical calibration function relating NERD BRFs to snow SSA and discuss measurement uncertainty.

3.3.1 Reflectance Measurement Validation

Using the NERD, we can obtain relatively accurate snow BRF measurements in nature without drastically affecting the snow. By recording measurements across two view azimuth angles and additional scattering planes by rotating the dome, we can assess azimuthal anisotropy in just a few minutes. Furthermore, by measuring multiple BRFs across multiple locations of a snow surface, we obtain numerous samples spanning multiple azimuthal planes that also enables easy characterization of the spatial variability in snow BRFs. Repeating rapid measurements in this manner allows us to obtain relatively accurate snow BRFs. Multiple precise measurements allow quantifying relatively large BRF variations associated with azimuthal anisotropy and spatial heterogeneity. Median BRFs reported across a unique wavelength, LED position, and photodiode zenith angle give a second-order approximation of the snow azimuthal-mean BRF. Computing RMS errors from these uniquely defined wavelength-BRF combinations quantifies measurement uncertainty. To this end, we first test NERD accuracy, precision, and responsivity by testing with idealized Lambertian surfaces before obtaining snow BRFs. Results in Table 1 indicate that any single NERD reading is subject to measurement uncertainty of about +/-2%. Although measurement uncertainty prevents us from using the NERD to obtain highly accurate BRFs, NERD BRF measurements are accurate and precise enough to observe relatively large variations in snow BRFs that are of particular interest in this study.

Compared to the Infrasnow (*Gergely et al.*, 2014), NERD BRF measurements of Lambertian surfaces are slightly less accurate. In a similar validation experiment,

Gergely et al. (2014) measure the reflectance of 0.25, 0.50, and 0.99 reflectance standards accurately to within less than 1%. In *Gergely et al.* (2014), an integrating sphere enables directional-hemispherical reflectance factor measurements at 950nm in contrast to the 1.30 and 1.55μm BRFs measured by the NERD. Both instruments make use of Lambertian reflectance standards for calibration and testing. Although each instrument uses a different wavelength and measures a different type of reflectance factor, testing on Lambertian reflectance standards with constant bidirectional reflectance distribution functions (BRDFs) allows for easy comparison of measurement uncertainty across multiple measurement techniques.

Dumont et al. (2010), for example, also use Lambertian reflectors and report a BRF measurement accuracy of better than 1% using a high angular resolution spectrogonioradiometer. *Gallet et al.* (2009) also make use of similar Lambertian standards to calibrate 1.31 and 1.55μm directional-hemispherical reflectance factor measurements. Using six standards, *Gallet et al.* (2009) parametrically fit signal voltages to reflectance values to account for nonlinear responsivity due to re-illumination of the standards through multiple scattering within the integrating sphere. While NERD responsivity is not perfectly linear, we expect re-illumination of the surface through multiple scattering within the black dome to be minimal.

Although photodiode responsivity varies with temperature, frequent calibration minimizes these errors. Therefore, the main source of NERD responsivity error is likely due to small deviations in light output from the LEDs. Like almost all electronic circuit elements, LED performance is also a function of its temperature. In its operational mode, the NERD drives the user-selected active LED with a current pulse width of two seconds. When the duty cycle is increased to 50% (two seconds on, two seconds off), we observe drift in the photodiode response. This responsivity drift is mitigated, but not completely eliminated, when the duty cycle is decreased to 20% (two seconds on, eight seconds off). Because we observe these responsivity errors in

testing shortly after calibration, we speculate that changing LED temperatures can affect the the light output enough to cause a one to two percent measurement error.

3.3.2 Monte Carlo Results

At 1.30 μm, 30 degree snow BRFs measured with the NERD for various snow SSA fall within the envelope of shape habits derived from Monte Carlo simulations. Monte Carlo simulations of spheres, droxtals, and hexagonal columns accurately predict 30 degree BRFs measured by the NERD for snow SSA ranging from 10 to 70 m^2/kg. Monte Carlo simulations predict lower BRF values at 60 degrees than at 30 degrees. These results provide an estimate of the uncertainty associated with deriving snow SSA from NERD BRFs across various shape habits and snow samples.

At 1.55 μm snow SSA values ranging from 10 to 70 m^2/kg yield lower Monte Carlo simulated BRFs than what is measured by the NERD. Comparing 30 and 60 degree viewing zenith angles, Monte Carlo results are more similar at 1.55 μm than at 1.30 μm. The relationships between 1.55 μm BRFs and snow SSA are also more linear than those at 1.30 μm. Stronger linearity at 1.55 μm, however, does not necessarily imply more accurate snow SSA retrieval. Obtaining snow SSA at 1.55 μm is more difficult due to the lesser span and lower responsivity of snow BRFs at this wavelength.

3.3.3 NERD Snow SSA Calibration

In general, snow SSA results from X-CT scans are related to NERD 1.30 μm nadir illuminated BRFs via an exponential relationship. This relationship exists at both the 30 and 60 degree viewing zenith angles. At 1.55 μm, snow SSA results from X-CT scans are related to NERD 15 degree, off-nadir illuminated BRFs via linear relationships. The relationship between snow SSA and NERD measurements is most clear and robust at 1.30 μm. Nadir illumination at 1.30 μm results in the best snow SSA agreement across NERD observations and Monte Carlo modeling at

the 30 degree viewing angle.

Our finding of the exponential relationship between snow SSA and 1.30 μm BRFs is consistent with previous studies. *Picard et al.* (2009) and *Gallet et al.* (2009), for example, also find exponential relationships between 1.31 μm reflectance and snow SSA. Likewise, *Gallet et al.* (2009) also identify a linear relationship between 1.55 μm reflectance and snow SSA. These studies, however, quantify snow SSA from hemispherical reflectances instead of BRFs. Hemispherical reflectance measurements theoretically reduce measurement variations associated with grain shapes. *Picard et al.* (2009) conclude that obtaining snow SSA from snow albedo measurements are subject to as much as 20 percent error when grain shape is unknown. This relatively large source of error due to grain shape is further explored here in Monte Carlo derived albedo calculations for snow surface of spheres, droxtals, solid hexagonal columns, and hexagonal plates (Figure 5).

As expected, snow modeled as spherical ice particles, simulated in the Monte Carlo model using the Henyey-Greenstein phase function

$$P_{\mathrm{HG}}(\cos\theta; g) = \frac{1 - g^2}{(1 + g^2 - 2g\cos\theta)^{3/2}}, \tag{3.7}$$

where θ is the scattering angle and g is the relevant asymmetry parameter, most closely agrees with 1.30 and 1.55 μm narrow band black-sky snow albedo calculated from the Snow, Ice, and Aerosol Radiation (SNICAR) model (*Flanner et al.*, 2007). Snow albedo dependence on grain shape is consistent at both wavelengths. In general, droxtals yield higher reflectances. Reflectances of solid hexagonal columns agree closely with spheres and SNICAR at both wavelengths for snow SSA lower than 40 m^2/kg, after which they tend toward reflectances similar to droxtals. Finally, hexagonal plates yield low reflectances. Low reflectances at both wavelengths are due to the extremely sharp forward scattering peak of these plates. Although highly

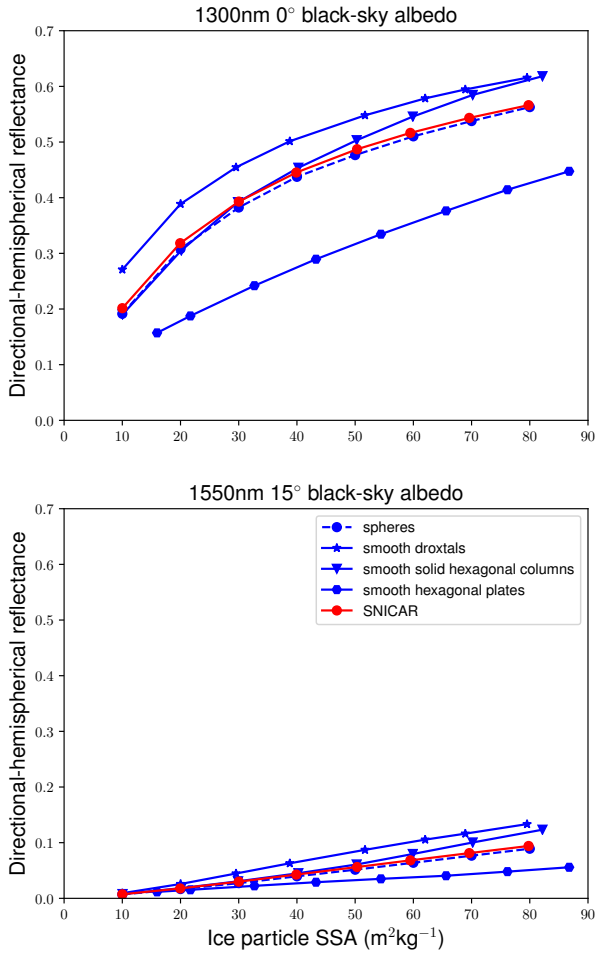

Figure 3.5: Modeled 1.30μm nadir (top) and 1.55μm 15 degree (bottom) directional-hemispherical reflectance for various snow SSA. Blue line segments connect albedo calculations from Monte Carlo simulations of photon pathways through snow mediums of spheres (circles, dashed lines), droxtals (stars), solid hexagonal columns (triangles), and hexagonal plates (hexagons). Red line segments connect albedo calculations from the Snow, Ice, and Aerosol Radiation (SNICAR) model (*Flanner et al.*, 2007).

idealized and perfectly smooth, these shape habits demonstrate the relatively large hemispherical reflectance variations across snow grain shape. These large variations in reflectance across grain shape are the largest source of uncertainty in snow SSA measurements using infrared reflectance. Monte Carlo modeling of BRFs in Figure 4 also suggest these uncertainties exist for directional reflectance measurements. These

uncertainties associated with unknown grain shape limit accuracy of NERD SSA retrieval.

Surprisingly, 1.55 μm BRFs measured by the NERD are higher than predicted by Monte Carlo modeling. Using the NERD, we observe 1.55 μm snow BRFs as high as 0.2. We measure the highest 1.55 μm snow BRFs at 60 degrees for particularly fresh snow, but high 1.55 μm BRFs are higher than models for all SSA. Because of its relatively high instrument precision (Table 1), these seemingly high BRFs are probably accurate. The primary contributor for the discrepancies against models at this wavelength is possibly due to the broad spectral emission characteristics of the 1.55μm LEDs. With full width at half maximums of 130nm, non-negligible light emission at wavelengths much lower, toward the near-infrared, is a likely cause of higher than expected reflectances. Although the spectral emission characteristics of NERD LEDs are simulated in Monte Carlo simulations using Gaussian photon wavelength distributions, and in SNICAR using a simple normalized Gaussian weighting function, non-negligible light emission from the tails of these distributions is possibly under estimated. Because of the expected sharp increase in snow reflectance as wavelength decreases from 1.55 to 1.30μm (*Wiscombe and Warren*, 1980; *Flanner et al.*, 2007), it is possible that even a small amount of light emission at wavelengths toward the near-infrared can have a measurable effect on snow BRF observations. This effect is further explored in Monte Carlo simulations by broadening the Gaussian distribution of photon wavelengths and in SNICAR by broadening the Gaussian weighting function applied to narrow-band albedo calculations. These calculations confirm this hypothesis, as 1.55 μm narrow band albedo with a full width at half maximums of 0.26 μm (doubled from 0.13 μm) closely agree with NERD BRF measurements. This finding suggests light emission from the 1.55 μm LEDs is non-negligible at lower, more absorptive wavelengths.

Notwithstanding the limitations associated with retrieving precise snow SSA from

BRFs, we generate an analytical calibration function relating snow SSA to NERD BRFs. To this end, we propose the general exponential form for 1.30 μm snow BRFs, such that

$$\text{SSA} = \alpha \exp(R_{1.30}) + \beta \tag{3.8}$$

for predicted snow SSA and 1.30 μm snow BRF $R_{1.30}$. Using least squares regression analysis, we compute parameters α and β for both 30 and 60 degree viewing zenith angles. At 30 degrees, setting $\alpha = 88.7$ and $\beta =$ -103 minimizes residuals and results in a snow SSA RMS error of 7.05 m^2/kg (Figure 6, left). At 60 degrees, setting $\alpha =$ 91.7 and $\beta =$ -113 minimizes residuals and results in a snow SSA RMS error of 7.23 m^2/kg (Figure 6, right).

This margin of uncertainty regarding SSA retrieval from snow infrared reflectance measurements falls within the expected range reported in previous studies (*Picard et al.*, 2009; *Gallet et al.*, 2009). This analysis complements previous studies and indicates that retrieval of highly precise snow SSA using NERD measurements is unlikely. Obtaining approximate estimates of snow SSA using NERD measurements across a wide variety of snow types, however, is highly likely. Because of its non-destructive nature, rapid, repeatable retrieval of approximate snow SSA using the NERD will be useful for studying hourly-scale snow metamorphosis (Figure 7). While the 1.30 μm, 30 degree viewing zenith angle BRF combination most closely agrees with modeled BRFs, a similar margin of error at the 60 degree viewing zenith angle can provide a second estimate of snow SSA. Reporting two snow SSA values using both view angles can ultimately give observationalists an idea of the variability in SSA retrieval resulting from the angular dependence of the snow BRDF in the near-infrared.

While these results minimize the usefulness of obtaining snow SSA from 1.55 μm snow BRFs, it is worth noting that *Gallet et al.* (2009) recommend using this wavelength in their DUFISSS to obtain snow of large SSA ($> 60 m^2$/kg). Here, nearly

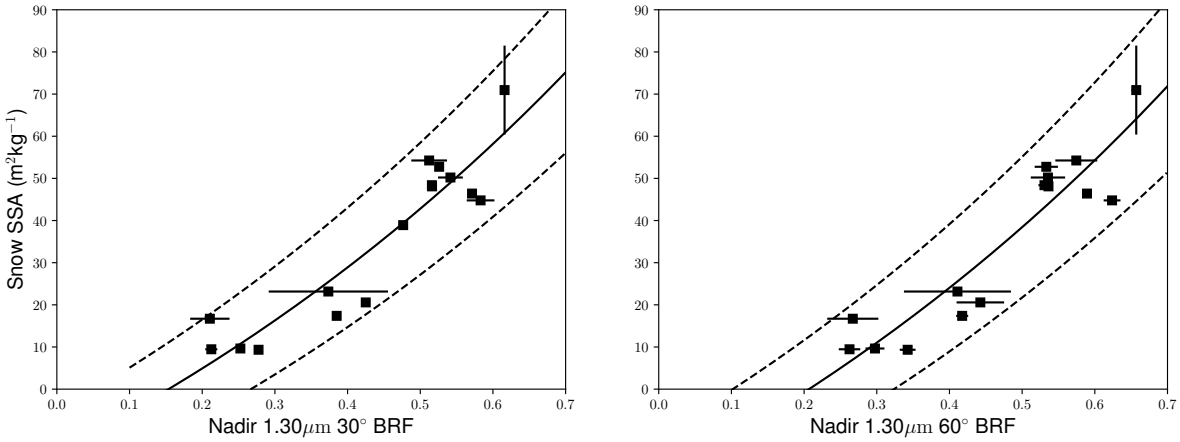

Figure 3.6: Near-Infrared Emitting and Reflectance-Monitoring Dome (NERD) snow specific surface area (SSA) calibration. Markers represent scattered X-CT derived snow SSA against nadir 1.30μm 30 (left) and 60 (right) degree bidirectional reflectance factors (BRFs) measured by the NERD (also plotted in Figure 4). Curves show center (solid), top and bottom (dashed) estimates of the analytical expression in equation 8. These are calculated from three α parameters (88.7+/- 9.50 m^2/kg at 30 degrees; 91.7+/- 10.13 m^2/kg at 60 degrees) using least squares regressions and their associated standard errors of the gradients (i.e., slopes).

all snow samples used in the NERD SSA calibration were lower than this threshold. A possible follow on study would include snow of higher SSA to determine the utility of 1.55 μm snow BRFs in measuring fresh snow of extremely high SSA particularly common in the extremely cold Arctic and Antarctic environments (*Legagneux et al.*, 2002; *Libois et al.*, 2015).

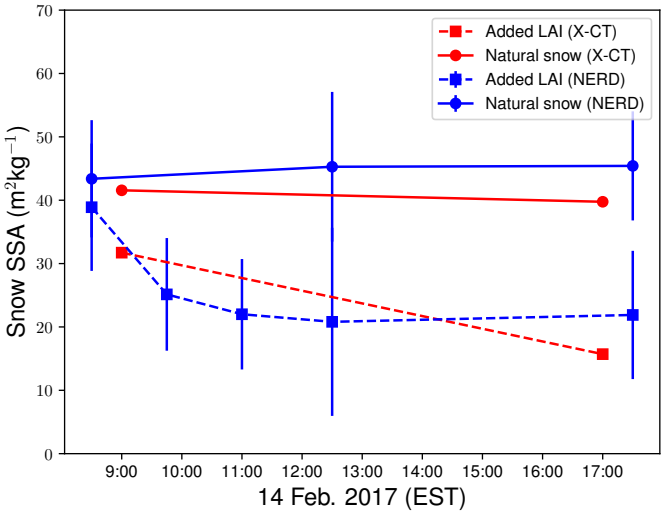

Figure 3.7: Snow specific surface area (SSA) measured throughout the day on February 14, 2017. Morning (9AM) and afternoon (5PM) samples were transported to the nearby Cold Regions Research Engineering Laboratory (CRREL) in Hanover, New Hampshire for X-ray microcomputed tomography (X-CT) analysis. SSA measurements derived from X-CT scans are shown in red. In blue, NERD SSA estimates derived from 1.30µm 60 degree BRFs (equation (8)) depict hourly-scale snow metamorphosis. Dashed line segments connect evolving snow SSA estimates of snow samples with added dust to induce rapid snow metamorphosis. Vertical error bars on NERD SSA estimates represent margin of uncertainty associated with calibration error plus measurement standard deviations. These results contain the first measurement data obtained by the NERD used to determine snow SSA. Because of its non-destructive nature, this technique enables the study of snow metamorphosis in situ on hourly time scales.

3.4 Conclusions

To obtain quick, accurate, reliable, and repeatable measurements of snow SSA, we engineered an instrument that measures snow 1.30 and 1.55µm BRFs. By flashing narrow band LEDs centered around these wavelengths, light reflected by experimental snow surfaces is measured using photodiodes mounted at 30 and 60 degrees relative to nadir. Photodiode currents are converted into measurable voltage signals enabling calibrated BRF calculations using Lambertian reflectance targets. Monte Carlo modeling and X-CT derived snow SSA help to demonstrate the relationship

between snow BRFs and SSA. Generally, we found an exponential relationship between 1.30μm BRFs and snow SSA. These results demonstrate the NERDs ability to obtain estimates of snow SSA to within +/- 7 m^2/kg without destroying snow samples. This non-destructive technique for snow SSA retrieval will be useful in science applications that investigate hourly-scale monitoring of snow SSA. Applying the NERD will be especially useful in experiments designed to learn about the effects of LAI on snow metamorphosis and to explore the spatial heterogeneity of snow SSA. Because it can operate quickly, NERD measurements will also complement satellite borne observations during narrow sampling windows.

CHAPTER IV

In Situ Observations of Snow Metamorphosis Acceleration Induced by Dust and Black Carbon

Abstract:

Snow metamorphosis directly affects solar absorption at the Earth surface. Furthermore, light absorbing impurities (LAI) within the snow (e.g., dust and black carbon particles) can dramatically alter snow albedo through direct and indirect darkening of the surface. The extent to which these LAI can accelerate snow metamorphosis, however, is challenging to assess in situ as common measurement techniques are destructive or require expensive, heavy equipment. To further investigate how LAI influence snow metamorphosis, we deployed two Near-Infrared Emitting and Reflectance-Monitoring Domes to monitor hourly-scale snow SSA in a series of LAI-in-snow experiments during a field campaign in Hanover, New Hampshire. Our results show more rapid decreasing snow SSA in snow with added LAI compared to natural (clean) snow. These results indicate that LAI deposition can accelerate snow metamorphosis and enhance positive snow internal albedo feedback, especially during cloud free, calm weather conditions when surface air temperatures are just below freezing. Although a complete understanding of the effects of LAI on snow metamorphosis requires further surface temperature, solar irradiance, and impurity concentration measurements, these results suggest that enhanced solar absorption

within the snow due to the presence of LAI drives positive albedo feedback conducive to accelerating snow metamorphosis.

4.1 Introduction

The cryosphere contains Earth's most reflective surfaces in snow and sea-ice cover. Fresh, dry snow, for example, reflects up to 90 percent of incident solar energy. In contrast, the Earth reflects on average roughly 30 percent of incident solar energy back to space. This sharp contrast between Earth's average planetary albedo and the more reflective cryosphere causes the presence of snow and ice cover to have a large effect on the Earth's total energy budget. *Flanner et al.* (2011) estimate that the presence of cryosphere surface elements, i.e., snow and sea-ice cover, reduces the absorbed solar energy flux by an average of 2.2 to 4.6 Wm^{-2} in the Northern Hemisphere. They also report a 30-year decrease in this cryosphere radiative effect of 0.45 Wm^{-2}, suggesting that the rapid loss of Arctic sea-ice cover (*Stroeve et al.*, 2012) and reduced Northern Hemisphere snow extent (*Dery and Brown*, 2007; *Derksen and Brown*, 2012) are increasing solar absorption. Increasing absorbed solar energy warms the Earth's surface which further reduces snow and sea-ice extent in a process known as the snow and ice albedo feedback.

As snow ages, its physical structure changes. This process of snow metamorphosis alters the snow specific surface area (SSA) (*Flanner and Zender*, 2006; *Wang and Baker*, 2014; *Ebner et al.*, 2015). Snow SSA is the total ice surface area S to mass m ratio, expressed in terms of its total ice volume V such that,

$$\mathrm{SSA} = S/m = \frac{S}{\rho_i V}, \tag{4.1}$$

where ρ_i is the density of pure ice (917 $\mathrm{kg/m}^3$ at 0° C). Snow SSA is an important physical property that strongly affects absorption of infrared radiation. Studies that

model the relationship between snow SSA and infrared reflectance (*Wiscombe and Warren*, 1980; *Flanner et al.*, 2007) typically refer to snow effective radius RE, where spheres of radii RE represent spherical snow grains with SSA = $3/(\rho_i \mathrm{RE})$. These studies demonstrate a strong dependence of near and shortwave infrared reflectance on snow grain RE, a relationship that is also observed in snow reflectance measurements (*Domine et al.*, 2006; *Gallet et al.*, 2009). Generally, as snow SSA decreases, near and shortwave infrared reflectance decreases. Previous studies monitor isothermal snow (*Ebner et al.*, 2015) and high temperature gradient (*Pinzer and Schneebeli*, 2009) snow metamorphosis, shedding light on the natural physical processes that drive decreasing snow SSA. In isothermal snow, highly faceted snow grains with relatively high SSA and low radii of curvature undergo coarsening in a process driven by the Kelvin effect. The diffusion of vapor in snowpacks with high temperature gradients can also drive snow metamorphosis that causes snow SSA to decrease. *Domine et al.* (2009), however, observe increasing snow SSA due to the fragmentation of surface snow grains mobilized by wind.

While snow metamorphosis relating to snow SSA effects near-infrared absorption most strongly, numerous studies verify the direct darkening of snow by the presence of light absorbing impurities (LAI) apparent in the visible spectrum (*Warren and Wiscombe*, 1980; *Flanner et al.*, 2007, 2009; *Hadley and Kirchstetter*, 2012; *Skiles and Painter*, 2017). Common LAI in snow include black / elemental carbon (BC), brown carbon, and dust, all of which play an important role in the climate system. These LAI have powerful direct and indirect effects that are large sources of uncertainty in the Intergovernmental Panel on Climate Change fifth assessment report climate change projections (*Ramanathan and Carmichael*, 2008; *Bond et al.*, 2013; *Qian et al.*, 2015). *Bond et al.* (2013) extensively review the role of BC in the climate system and estimate emission totals by region and source, identifying three major source categories: open biomass burning, especially prevalent in African grass and woodland

burning, residential solid fuel burning, used especially throughout Asia and Africa for cooking, and diesel fuel burning used worldwide. Other sources include residential and industrial coal burning power and forest fires. 100ppb BC in snow is enough to reduce snow albedo by up to 10 percent depending on snow RE (*Warren and Wiscombe*, 1980; *Flanner et al.*, 2007, 2009; *Hadley and Kirchstetter*, 2012). *Hadley and Kirchstetter* (2012) verify what *Warren and Wiscombe* (1980) and the widely used Snow, Ice, and Aerosol Radiation (SNICAR) model (*Flanner et al.*, 2007, 2009) predict in that snow albedo reduction by BC is enhanced for larger snow RE. The enhancement of snow darkening by BC for larger snow RE is a source of positive albedo feedback in cases when the LAI accelerate snow metamorphosis. This positive snow metamorphosis / albedo feedback, however, is not verified experimentally and it is unclear how solar heating of snow by LAI affect other metamorphosis processes studied by *Flanner and Zender* (2006), *Wang and Baker* (2014), and *Ebner et al.* (2015).

Positive snow metamorphosis / albedo feedback is initiated by LAI when enhanced absorption of solar radiation results in decreasing snow SSA. Decreasing snow SSA directly increases the absorbed solar radiation and indirectly increases the albedo reduction attributable to LAI. If further warming is conducive to further decreasing snow SSA, then positive feedback will drive unstable snow metamorphosis. Without compensating negative feedback mechanisms, snow metamorphosis can lead to melting at the surface which can redistribute LAI and completely change the snow surface structure. In theory, however, surface warming weakens the snow temperature gradient and suppresses grain growth processes explained by (*Flanner and Zender*, 2006). The net effect of these competing feedback mechanisms is unknown and difficult to study in nature because measurement techniques easily disturb the natural snow structure.

The purpose of this study is to demonstrate rapid snow metamorphosis caused by

LAI deposition. After depositing LAI on freshly fallen snow, rapid snow metamorphosis of decreasing snow SSA is indicative of dominant positive snow metamorphosis / albedo feedback. In this study, we observe snow metamorphosis from freshly fallen snow of relatively high SSA to aged snow of low SSA. Using our Near-Infrared Emitting and Reflectance-Monitoring Dome (NERD), we measure hourly-scale temporally evolving 1.30 and 1.55μm snow bidirectional reflectance factors (BRF) during LAI induced metamorphosis. We supplement NERD BRF measurements using X-ray microcomputed tomography (X-CT) to calculate snow SSA. We measure snow BRFs of natural snow (control) and manually deposited LAI-contaminated snow (experimental) plots and evaluate the effect of added LAI on snow metamorphosis. Experimental plots undergo rapid metamorphosis while control plots remain mostly unchanged. Experimentally induced snow metamorphosis by heavy BC and dust loading is evident from decreasing snow infrared reflectance throughout the day and a decrease of snow SSA confirmed by X-CT. We hypothesize that LAI induces positive feedback and accelerates snow metamorphosis. Generally, our experiments confirm this hypothesis. Atmospheric conditions, however, including cloudiness, wind speeds, and surface temperature can obscure these effects. This study demonstrates conditions for which snow metamorphosis can be enhanced by the presence of LAI.

4.2 Materials and Methods

Snow 1.30μm, nadir illuminated BRFs are measured at 30 and 60 degrees relative to zenith. These BRFs are obtained using the Near-Infrared Emitting and Reflectance-Monitoring Dome (NERD), an instrument designed to quickly and accurately retrieve snow grain size (Chapter 3). Snow grain size is monitored throughout the day in a series of dust- and soot-in-snow experiments. Two types of LAI are deposited onto experimental snow plots in an open field in Hanover, New Hampshire during February 10 and February 17 experiments. On February 10, surface temper-

atures ranged from -14 to -9 °C. Low to moderate wind speeds were observed from the early morning hours through the afternoon. During the day, partly to mostly cloudy conditions were observed. On February 17, surface temperatures ranged from -4 to +2 °C. Wind speeds and cloud cover were minimal making way for calm, clear sky conditions. LAI deposited onto experimental snow included hydrophobic black carbon and sand particles, which are sifted multiple times to filter out larger particles. After sifting, filtered BC and sand particles are sprinkled onto plots to mimic large deposition events.

In each experiment, snow BRFs are measured multiple times throughout the day. Monitoring hourly-scale BRFs of snow during the day enables the observation of solar-heating induced snow metamorphosis. For each experiment, one square meter plots of snow are designated as natural (control) or contaminated (experimental). In experiment one (February 10), contaminated plots are loaded with BC until visible darkening is apparent. In experiment two (February 17), just a pinch of BC and 30g of sand are applied to each experimental plot. These values are selected to mimic extreme LAI deposition events observed by *Skiles and Painter* (2017).

In the February 10 experiment, BC is deposited onto the experimental plot after snow accumulation the previous day. Beginning at midnight, measurements are conducted at about 12:00am, 3:00am, and 6:00am to monitor snow metamorphosis without solar heating. After sunrise, measurements are continued into the daytime hours. For each set of measurements, 30 degree and 60 degree BRFs are both recorded four times. BRFs are measured over two different locations within each experimental plot with two photodiodes at each viewing angle (30 and 60 degrees). Thus, each datum represents the mean of four samples which also gives an idea of the variability across each set of measurements.

The February 17 experiment is set up in a similar manner. After fresh snow accumulation on February 15, BC and dust is deposited onto experimental plots. On

February 16, data collection is difficult due to high wind speeds, so the experiment is set up again on the morning of February 17. Measurements are conducted on four experimental plots, two that are set up on February 16, and two that are set up on February 17.

4.3 Results and Discussion

Added BC and dust accelerate the process of snow metamorphosis from fresh snow of relatively high SSA to snow of lower SSA. Snow metamorphosis in experimental plots containing added LAI is apparent under direct solar irradiance at surface temperatures just below freezing. Measurements collected at initial application of LAI show minimal direct darkening of snow from LAI at 1.30 and 1.55μm (Fig. 1, top). Decreasing 1.30 and 1.55μm BRFs soon after solar heating in experimental plots but not in natural snow demonstrates the indirect effect of LAI on snow through more rapid snow metamorphosis. X-CT measurements verify that snow SSA also decreases (bottom) which directly reduces the solar broadband albedo of the snow. The reduction of snow broadband albedo has larger consequences in the total surface energy budget as increasing absorbed solar radiation within the snow itself can lead to additional surface melting via the snow albedo feedback.

We use the February 17 experiment to monitor snow metamorphosis occurring after forced large BC and dust deposition events. Typical BC deposition events are very small, so it is difficult to reproduce natural BC concentrations when adding any BC to a one square meter plot. We attempt to make measurements on February 16, but windy, cloudy conditions obstruct data collection. It is difficult to obtain NERD measurements during the daytime in cloudy, diffuse lighting conditions. This is because subsurface scattering of diffuse light is difficult to block. The photodiode amplifiers on the NERD saturate when there is too much background lighting. More importantly, cloudy conditions completely obscure enhanced snow SSA meta-

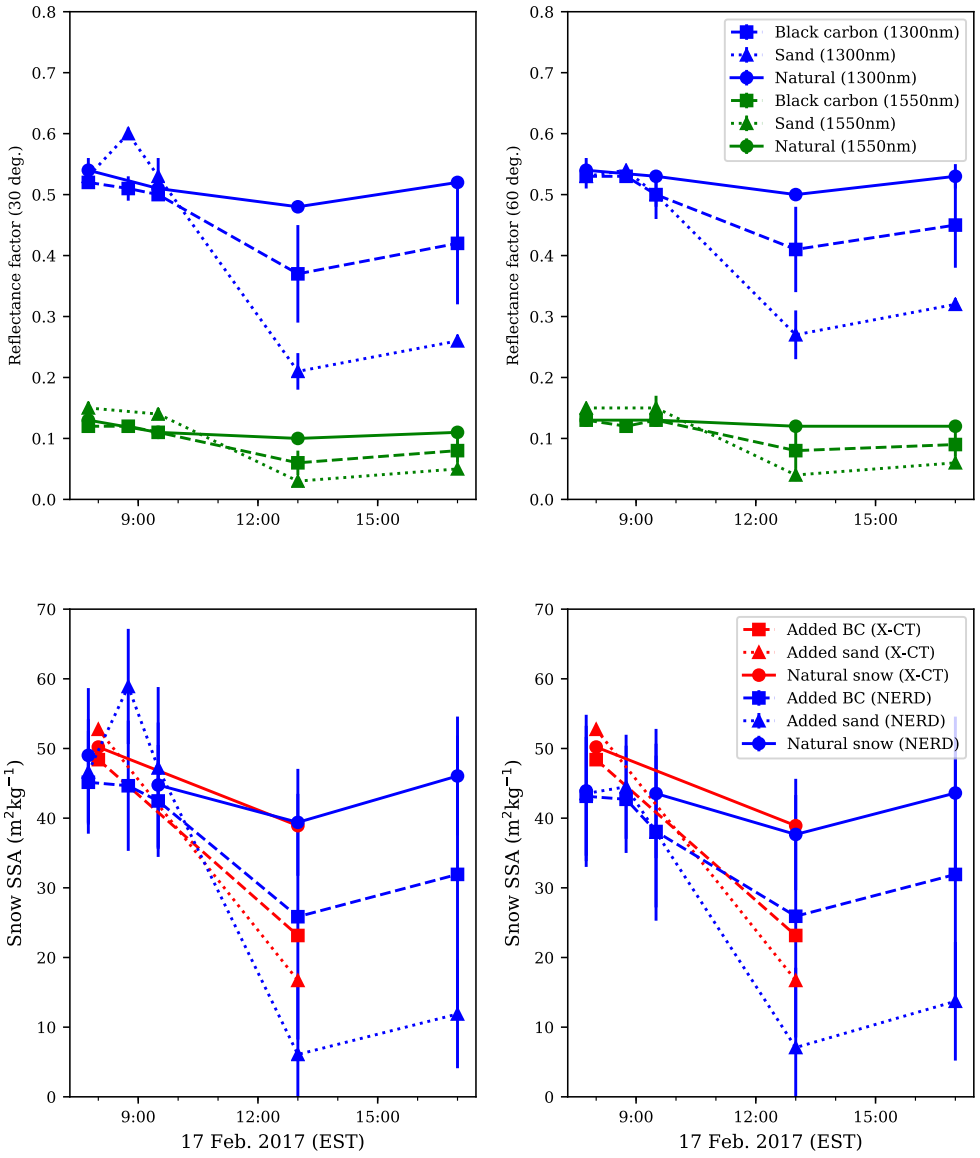

Figure 4.1: Evolution of snow BRFs (top) and SSA (bottom) throughout the February 17 experiment. Solid lines connect measurement data from natural snow. Dashed lines connect measurement data from experimental plots contaminated with added BC. Dotted lines connect measurements from contaminated plots with added sand. In the top figure, blue (green) curves represent 1.30µm (1.55µm) BRFs at 30 (left) and 60 (right) degrees. In the bottom figure, blue curves represent NERD-estimated SSA while red curves represent SSA derived from X-CT. In all cases, experimental snow plots with added LAI, especially 30g of sand (dotted), evolve more quickly under direct solar irradiance than natural snow plots (solid).

morphosis (Figure 2). This is apparent in the February 10 control experiment, where minimal metamorphosis occurs despite heavy BC loading. The lack of metamorphosis on February 10 is a direct consequence of windy, cloudy conditions that mobilize BC particles off the experimental plot and also block direct solar illumination. The February 10 experiments are also in a well shaded location, where tall trees block much of the direct solar irradiance from being absorbed by BC. On the morning of February 17, two additional experimental plots are set up in the exact same manner as the February 16 plots. Under a calm, clear atmosphere, conditions are ideal to observe LAI induced metamorphosis and collect data with the NERD. As expected, rapid metamorphosis begins in all four experimental plots after 10:00am local time, but not in natural snow. These results suggest that LAI deposition induces net positive snow metamorphosis / albedo feedback.

Positive snow metamorphosis / albedo feedback is evident by rapidly decreasing snow BRFs at two infrared wavelengths in experimental versus control plots. The fastest metamorphosis occurs in the heavy dust loaded plot, suggesting that extreme, but realistic dust deposition events can quickly alter the snow state. The February 17 experiment is indicative of enhanced solar heating inducing snow metamorphosis, as BRFs decrease most rapidly during hours of peak insolation.

These results verify what is hypothesized from previous studies. Few studies examine hourly-scale snow metamorphosis in the presence of LAI in situ like this one, but positive snow metamorphosis / albedo feedback can be inferred from *Skiles and Painter* (2017) and *Adolph et al.* (2017) where they find that Colorado and New Hampshire snow albedo is dominated by dust concentration and snow grain size, respectively. Although these studies find different dominant influences on snow albedo (i.e., dust concentration versus snow grain size), both of these relationships enable positive albedo feedback within snow.

Because snow albedo is directly related to snow SSA and dust concentration, pos-

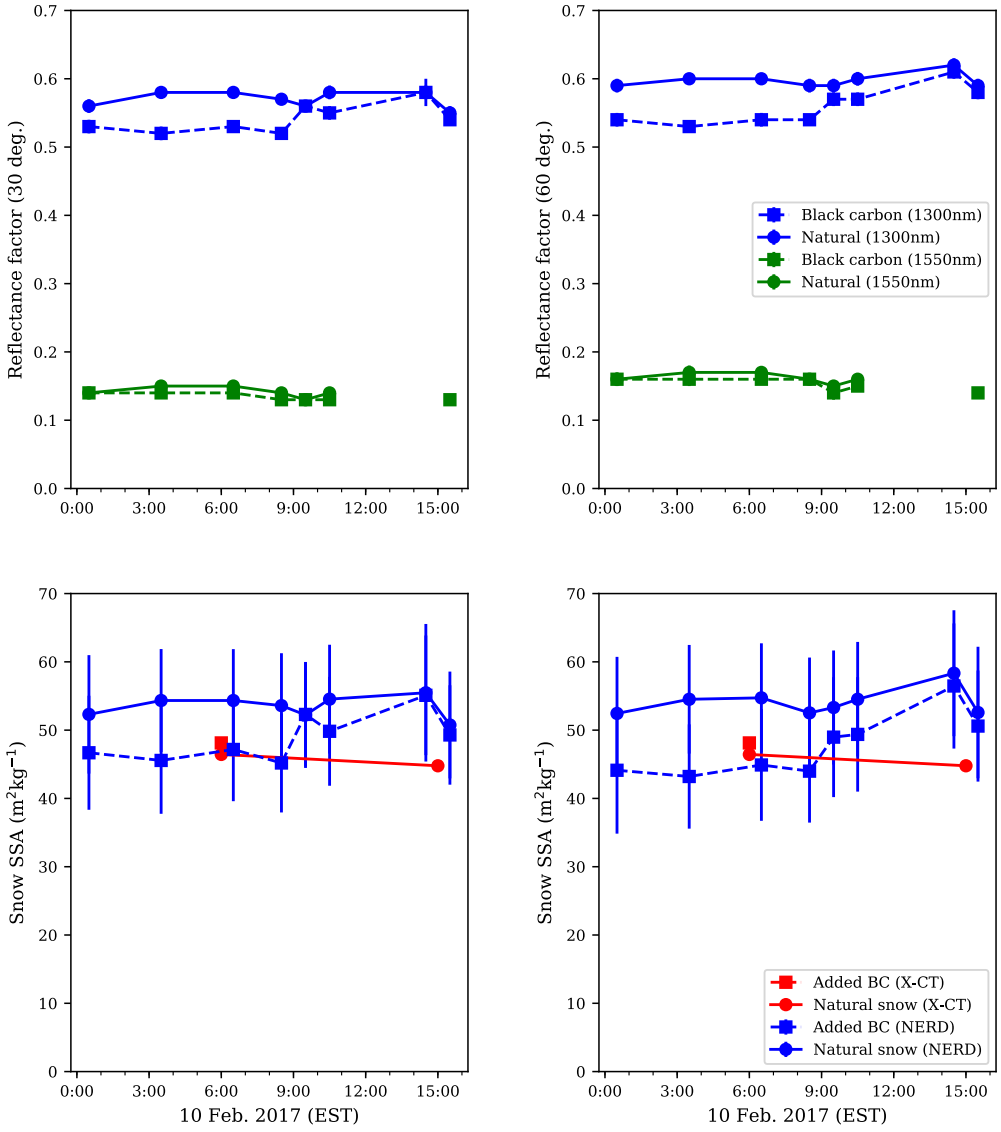

Figure 4.2: Evolution of snow BRFs (top) and SSA (bottom) throughout the February 10 experiment. As in figure 1, solid lines connect measurement data from natural snow while dashed lines connect measurement data from experimental plots contaminated with added BC. In the top figure, blue (green) curves represent 1.30µm (1.55µm) BRFs at 30 (left) and 60 (right) degrees. In the bottom figure, blue curves represent NERD-estimated SSA while red curves represent SSA derived from X-CT. Cloudy, windy conditions prevent observable LAI induced snow metamorphosis. Overnight measurements and cloud cover make for a good control experiment with minimal snow aging.

itive surface albedo feedback initiated due to the presence of LAI occurs when solar heating of the surface induces snow melt. In these experiments, LAI enhances solar absorption at the surface which warms the snowpack. As the snow surface begins to melt, near-infrared reflectance decreases rapidly. Rapidly decreasing near-infrared reflectance is indicative of either the accumulation of liquid water from melting snow or decreasing snow SSA. In the former case, the presence of liquid water at the surface enhances near-infrared absorption which further warms the surface and drives additional snow melt. In the latter case, decreasing snow SSA enhances near-infrared absorption and decreases snow broad-band albedo which also enhances the absorbed energy content of the snow surface. X-CT scans confirm that snow SSA decreases more rapidly in contaminated snow versus natural snow. These scans verify that SSA decreases from morning to afternoon, but cannot determine whether or not the presence of liquid water played a major role in the metamorphic process. Visual inspection of the snow, guided with a gentle touch with a gloved hand, provide qualitative evidence of liquid water present in contaminated snow during peak insolation. In either case, decreased snow SSA toward the end of the day, as evidenced by NERD measurements and X-CT scans, indicate that adding LAI to the snow surface accelerates positive snow metamorphosis / albedo feedback. This accelerated feedback due to the presence of dust and BC demonstrates the important, delicate role LAIs have in snow melt and snow albedo.

The other important influence on the strength of the snow metamorphosis / albedo feedback is the surface air temperature. LAI induced snow metamorphosis has the strongest effect in clear sky conditions when the surface air temperature is close to but not exceeding 0° C. When surface air temperatures are just below freezing, clean fresh snow is still reflective enough to limit melting which could otherwise induce positive albedo feedback. LAI-contaminated snow, however, absorbs enough solar radiation to initiate the rapid metamorphosis observed in this study. The divergence

of snow surface behavior between control and experimental plots in these conditions demonstrates the powerful effects of LAI in snow in sunny, warm, sub-freezing conditions. To better determine surface air temperature regimes for which these effects are most pronounced, a follow on study would reproduce these experiments across a broader range of conditions. Expanding this study for lower temperatures, coupled with incident radiation measurements, would provide results that could further our understanding of positive snow metamorphosis /albedo feedback in snow with more extreme temperature gradients. Determining conditions for which a weakened temperature gradient, due to enhanced solar absorption at the snow surface, could inhibit snow metamorphosis via negative feedback, for example, would be of high value to the snow modeling community.

4.4 Conclusions

These experiments demonstrate snow metamorphosis induced by LAI. Snow metamorphosis occurs in naturally aging snow, but the indirect radiative effects from LAI have unknown consequences. Here, we used the NERD to measure BRFs to monitor the evolution of snow SSA under different LAI loads. We learned that LAI induced snow metamorphosis occurs rapidly under ideal conditions. That is, a cloud free atmosphere with surface temperatures near, but not above, freezing yields apparent divergence in the snow surface state. In these conditions, clean snow maintains relatively high SSA compared to the rapid reduction of snow SSA when LAI absorbs direct sunlight. Snow BRFs measured by the NERD demonstrate the rapid change in the snow state, an observation that was also visibly apparent to the naked eye.

These experiments confirm what has been hypothesized previously. That is, the deposition of LAI has potential to accelerate snow metamorphosis through positive snow albedo feedback. Until now, it has only been speculated that positive feedback would be the dominant feedback mechanism relative to possible negative feedbacks

that could occur due to weakening temperature gradients. These experiments provide verification of positive feedback accelerating snow metamorphosis in outdoor snow. This conclusion will help microphysical snow modeling efforts, but future experimentation will expand on the environmental conditions. Repeating similar experiments in different conditions, including a wide range of surface temperature and incident light conditions, will be helpful in expanding the utility of our findings. Additionally, using smaller amounts of LAI will further our understanding of these processes through sensitivity testing. We demonstrated the effects of extreme LAI contamination on snow in ideal conditions to observe rapid snow metamorphosis. Using smaller LAI loads in various conditions, however, will increase the utility because it will inform on the indirect effects of LAI in snow for a wider range of conditions.

CHAPTER V

Conclusion: Earth's Cryosphere Albedo Feedback

This dissertation investigates snow and ice albedo feedback from the global scale down to the micro-scale. On the global scale, surface albedo feedback operates in transient climate as Earth's ice cover adjusts to an external forcing. In todays climate, this external forcing is a radiative forcing due to the increasing greenhouse gas concentrations primarily from carbon dioxide and methane. The buildup of these gases reduces Earth's outgoing long-wave radiation. The equilibrium response to this forcing is an increase in Earth's effective emission temperature. This response continues until Earth's energy balance equation (1.1) is satisfied. At the surface, this translates to an increase in global mean temperature. Increasing surface temperatures near ice cover boundaries eventually lead to long term decreases in global ice cover. Recent studies, for example, confirm the rapid decline in Arctic perennial sea-ice cover over the last 30-50 years. Because ice is particularly reflective in the solar spectrum, these large scale declines in sea-ice cover directly reduce Earth's surface albedo. The reduction of Earth's surface albedo is propagated to the TOA, though this affect is somewhat mitigated by cloud cover. Nevertheless, it is confirmed that the rapid reduction in Arctic sea-ice cover over the last three decades resulted in a decline of the planetary albedo observed at the TOA. Finally, the reduction in planetary albedo directly enhances Earth's absorption of solar energy. This destabilizes the planetary

energy budget resulting in further equilibrium climate response. Independently, this positive feedback, known as the ice albedo feedback, operates until Earth's surface albedo stabilizes. This positive feedback mechanism results in removal of perennial Arctic (and Antarctic) ice cover in a warming climate.

5.1 Research Summary

The research presented here picks up on this discussion of ice albedo feedback and seeks to identify when and if run-away albedo feedback occurs in future transient climate simulations. To this end, we developed a new framework for quantifying time-dependent surface albedo feedback (SAF) on decadal timescales. In summary, we find that SAF strengthens in 16 of 29 climate models during 21st century RCP8.5 transient future climate simulations. Quantifying SAF on decadal timescales enables assessing time-dependent variations in the strength of this feedback within 21st century simulations across a wide set of climate models. To our surprise, multi-model results show no apparent weakening in SAF strength despite a reduction in the mean Arctic sea-ice extent as the 21st century progresses. With there being less sea-ice in the models, we expected SAF strength to lessen toward the end of the century as less overall capacity for SAF persists on the global scale. On the contrary, however, the rapid reduction in Arctic sea-ice extent, as simulated by almost all CMIP5 models under the extreme RCP8.5, does not result in a reduction in the global SAF. Extended simulations through 2300 show a peak in the strength of global scale SAF around 2150, after which it monotonically decreases to near zero by 2300 (*Schneider et al.*, 2018).

Next, we zoom in from the global scale down to the micro scale to explore micro-physical albedo feedback within snowpacks. We found that positive SAF also happens on micro-physical scales. Light interaction within the snowpack changes substantially as snow ages (*Flanner and Zender*, 2006). To study this process of snow metamorpho-

sis, we developed an instrument capable of measuring snow specific surface area (SSA) called the Near-Infrared Emitting and Reflectance-Monitoring Dome (NERD). Pulsing light emitting diodes mounted in a black dome enables bidirectional reflectance factor measurements at 1.30 and 1.55 μm using photodiode amplifier circuits. Because of its light weight, 9V-battery powered design, the NERD is especially portable and rugged, making it a useful tool for studying hourly-scale snow metamorphosis. Furthermore, because of its non-destructive nature, we applied the NERD to study snow metamorphosis in a series of LAI in snow experiments. In comparing natural snow to experimental snow plots with added LAI, we identified rapid snow metamorphosis in experimental snow plots. Using the NERD, we discovered time evolving, decreasing snow SSA throughout a series of day time experiments in snow with added LAI, but not in natural snow. This divergence in physical snow properties is indicative of the indirect darkening effect LAI have on snow. Dynamic snow SSA throughout direct sun exposure demonstrated positive albedo feedback induced by LAI.

5.2 Future Direction

Moving forward, further study is necessary to ultimately improve the representation of the snow metamorphosis albedo feedback in global climate models. In particular, similar LAI-in-snow studies carried out with known impurity concentrations would be helpful in quantifying the non-linear processes driving LAI induced snow metamorphosis. Furthermore, extending measurements beneath the surface, through the use of snow pits, would give snow SSA profiles to better our understanding of the entire snowpack evolution. Reproducing similar studies with added LAI more representative of that occurring in nature would more similarly represent natural snow aging. Finally, a complete description of LAI particle size distributions and species would provide experimental case studies applicable to a broad range of environments. Future studies carried out with these added measurements across several

environments, ranging from those in polar regions to those in high altitude regions, is a complete approach from the in situ measurement perspective. Ultimately, results from these studies should be compared with simultaneous satellite borne observations. The coupling of in situ measurement campaigns, made possible with use of the NERD, and remote sensing observations would be useful for measurement validation and would provide scientific knowledge helpful to the modeling community.

APPENDICES

APPENDIX A

CESM1-CAM5 Radiative Kernel

In *Schneider et al.* (2018), a new radiative kernel from the CESM1-CAM5 configuration is generated using a similar approach presented by *Perket et al.* (2014). The fully coupled (active land, atmosphere, ocean and river models with prognostic sea ice) CESM1-CAM5 configuration is run for two years with a finite volume grid. For each model timestep, the radiative transfer scheme is conducted twice: once normally and once with a perturbed albedo. The radiative kernel is then obtained by dividing the difference in radiative fluxes by the difference in albedos. To regrid the native resolution of each radiative kernel to each model's resolution, a bivariate spline approximation is used to linearly interpolate the kernels. After interpolation, the radiative kernels represent the monthly estimate of each model grid-cell's net effect on the TOA irradiance caused by a one percent change in surface albedo.

APPENDIX B

Effective radii equivalence for convex bodies

The objective of this appendix is to show that for convex bodies, sphere effective radii r_{eff}, as defined in (3.2), and RE, as defined in (3.3), are equivalent. *Vouk* (1948) shows that for convex bodies,

$$S = 4\bar{A}, \tag{B.1}$$

where $\bar{A}$ is the average projected area of the convex body. Substituting (B.1) into (3.1) then gives

$$\text{SSA} = \frac{4\bar{A}}{\rho_{ice} V}. \tag{B.2}$$

Equating (3.2) and (B.2) and simplifying,

$$3/r_{eff} = \frac{4\bar{A}}{V}. \tag{B.3}$$

Finally, solving (B.3) for r_{eff} gives

$$r_{eff} = \frac{3}{4}(V/\bar{A}), \tag{B.4}$$

which is equivalent to the expression for RE given in (3.3), thus concluding the proof.

BIBLIOGRAPHY

BIBLIOGRAPHY

Adolph, A. C., M. R. Albert, J. Lazarcik, J. E. Dibb, J. M. Amante, and A. Price (2017), Dominance of grain size impacts on seasonal snow albedo at open sites in New Hampshire: SEASONAL SNOW ALBEDO IN NEW HAMPSHIRE, *Journal of Geophysical Research: Atmospheres*, *122*(1), 121–139, doi:10.1002/2016JD025362.

Andry, O., R. Bintanja, and W. Hazeleger (2017), Time-Dependent Variations in the Arctics Surface Albedo Feedback and the Link to Seasonality in Sea Ice, *Journal of Climate*, *30*(1), 393–410, doi:10.1175/JCLI-D-15-0849.1.

Bond, T. C., S. J. Doherty, D. W. Fahey, P. M. Forster, T. Berntsen, B. J. DeAngelo, M. G. Flanner, S. Ghan, B. Krcher, D. Koch, S. Kinne, Y. Kondo, P. K. Quinn, M. C. Sarofim, M. G. Schultz, M. Schulz, C. Venkataraman, H. Zhang, S. Zhang, N. Bellouin, S. K. Guttikunda, P. K. Hopke, M. Z. Jacobson, J. W. Kaiser, Z. Klimont, U. Lohmann, J. P. Schwarz, D. Shindell, T. Storelvmo, S. G. Warren, and C. S. Zender (2013), Bounding the role of black carbon in the climate system: A scientific assessment: BLACK CARBON IN THE CLIMATE SYSTEM, *Journal of Geophysical Research: Atmospheres*, *118*(11), 5380–5552, doi:10.1002/jgrd.50171.

Budyko, M. I. (1969), The effect of solar radiation variations on the climate of the Earth, *Tellus*, *21*(5), 611–619, doi:10.1111/j.2153-3490.1969.tb00466.x.

Cao, Y., S. Liang, X. Chen, and T. He (2015), Assessment of Sea Ice Albedo Radiative Forcing and Feedback over the Northern Hemisphere from 1982 to 2009 Using Satellite and Reanalysis Data, *Journal of Climate*, *28*(3), 1248–1259, doi:10.1175/JCLI-D-14-00389.1.

Cavalieri, D. J., and C. L. Parkinson (2012), Arctic sea ice variability and trends, 1979–2010, *The Cryosphere*, *6*(4), 881–889, doi:10.5194/tc-6-881-2012.

Cohen, J., J. A. Screen, J. C. Furtado, M. Barlow, D. Whittleston, D. Coumou, J. Francis, K. Dethloff, D. Entekhabi, J. Overland, and J. Jones (2014), Recent Arctic amplification and extreme mid-latitude weather, *Nature Geoscience*, *7*(9), 627–637, doi:10.1038/ngeo2234.

Colman, R. A. (2013), Surface albedo feedbacks from climate variability and change: GCM ALBEDO FEEDBACKS, *Journal of Geophysical Research: Atmospheres*, *118*(7), 2827–2834, doi:10.1002/jgrd.50230.

Comiso, J. C. (2012), Large Decadal Decline of the Arctic Multiyear Ice Cover, *Journal of Climate*, *25*(4), 1176–1193, doi:10.1175/JCLI-D-11-00113.1.

Comiso, J. C., C. L. Parkinson, R. Gersten, and L. Stock (2008), Accelerated decline in the Arctic sea ice cover, *Geophysical Research Letters*, *35*(1), doi:10.1029/2007GL031972.

Crook, J. A., and P. M. Forster (2014), Comparison of surface albedo feedback in climate models and observations: Crook and Forster: Surface Albedo Feedback, *Geophysical Research Letters*, *41*(5), 1717–1723, doi:10.1002/2014GL059280.

Derksen, C., and R. Brown (2012), Spring snow cover extent reductions in the 2008-2012 period exceeding climate model projections: SPRING SNOW COVER EXTENT REDUCTIONS, *Geophysical Research Letters*, *39*(19), n/a–n/a, doi:10.1029/2012GL053387.

Dery, S. J., and R. D. Brown (2007), Recent Northern Hemisphere snow cover extent trends and implications for the snow-albedo feedback, *Geophysical Research Letters*, *34*(22), doi:10.1029/2007GL031474.

Dessler, A. E. (2013), Observations of Climate Feedbacks over 200010 and Comparisons to Climate Models*, *Journal of Climate*, *26*(1), 333–342, doi:10.1175/JCLI-D-11-00640.1.

Domine, F., R. Salvatori, L. Legagneux, R. Salzano, M. Fily, and R. Casacchia (2006), Correlation between the specific surface area and the short wave infrared (SWIR) reflectance of snow, *Cold Regions Science and Technology*, *46*(1), 60–68, doi:10.1016/j.coldregions.2006.06.002.

Domine, F., A.-S. Taillandier, A. Cabanes, T. A. Douglas, and M. Sturm (2009), Three examples where the specific surface area of snow increased over time, *The Cryosphere*, *3*(1), 31–39, doi:10.5194/tc-3-31-2009.

Donohoe, A., and D. S. Battisti (2011), Atmospheric and Surface Contributions to Planetary Albedo, *Journal of Climate*, *24*(16), 4402–4418, doi:10.1175/2011JCLI3946.1.

Dumont, M., O. Brissaud, G. Picard, B. Schmitt, J.-C. Gallet, and Y. Arnaud (2010), High-accuracy measurements of snow Bidirectional Reflectance Distribution Function at visible and NIR wavelengths comparison with modelling results, *Atmospheric Chemistry and Physics*, *10*(5), 2507–2520, doi:10.5194/acp-10-2507-2010.

Ebner, P. P., M. Schneebeli, and A. Steinfeld (2015), Tomography-based monitoring of isothermal snow metamorphism under advective conditions, *The Cryosphere*, *9*(4), 1363–1371, doi:10.5194/tc-9-1363-2015.

F.E. Nicodemus, J.C. Richmond, J.J. Hsia, I.W. Ginsberg, and T. Limperis (1977), Geometrical Considerations and Nomenclature for Reflectance.

Fernandes, R., H. Zhao, X. Wang, J. Key, X. Qu, and A. Hall (2009), Controls on Northern Hemisphere snow albedo feedback quantified using satellite Earth observations, *Geophysical Research Letters*, *36*(21), doi:10.1029/2009GL040057.

Flanner, M. G., and C. S. Zender (2006), Linking snowpack microphysics and albedo evolution, *Journal of Geophysical Research*, *111*(D12), doi:10.1029/2005JD006834.

Flanner, M. G., C. S. Zender, J. T. Randerson, and P. J. Rasch (2007), Present-day climate forcing and response from black carbon in snow, *Journal of Geophysical Research*, *112*(D11), doi:10.1029/2006JD008003.

Flanner, M. G., C. S. Zender, P. G. Hess, N. M. Mahowald, T. H. Painter, V. Ramanathan, and P. J. Rasch (2009), Springtime warming and reduced snow cover from carbonaceous particles, *Atmospheric Chemistry and Physics*, *9*(7), 2481–2497, doi:10.5194/acp-9-2481-2009.

Flanner, M. G., K. M. Shell, M. Barlage, D. K. Perovich, and M. A. Tschudi (2011), Radiative forcing and albedo feedback from the Northern Hemisphere cryosphere between 1979 and 2008, *Nature Geoscience*, *4*(3), 151–155, doi:10.1038/ngeo1062.

Flato, G., J. Marotzke, B. Abiodun, P. Braconnot, S. Chou, W. Collins, P. Cox, F. Driouech, S. Emori, V. Eyring, C. Forest, P. Gleckler, E. Guilyardi, C. Jakob, V. Kattsov, C. Reason, and M. Rummukainen (2014), Evaluation of Climate Models, in *Climate Change 2013 - The Physical Science Basis*, edited by Intergovernmental Panel on Climate Change, pp. 741–866, Cambridge University Press, Cambridge, dOI: 10.1017/CBO9781107415324.020.

Fletcher, C. G., H. Zhao, P. J. Kushner, and R. Fernandes (2012), Using models and satellite observations to evaluate the strength of snow albedo feedback, *Journal of Geophysical Research*, *117*(D11), doi:10.1029/2012JD017724.

Fletcher, C. G., C. W. Thackeray, and T. M. Burgers (2015), Evaluating biases in simulated snow albedo feedback in two generations of climate models, *Journal of Geophysical Research: Atmospheres*, *120*(1), 12–26, doi:10.1002/2014JD022546.

Gallet, J.-C., F. Domine, C. S. Zender, and G. Picard (2009), Measurement of the specific surface area of snow using infrared reflectance in an integrating sphere at 1310 and 1550 nm, *The Cryosphere*, *3*(2), 167–182, doi:10.5194/tc-3-167-2009.

Gallet, J.-C., F. Domine, and M. Dumont (2014), Measuring the specific surface area of wet snow using 1310 nm reflectance, *The Cryosphere*, *8*(4), 1139–1148, doi:10.5194/tc-8-1139-2014.

Gergely, M., F. Wolfsperger, and M. Schneebeli (2014), Simulation and Validation of the InfraSnow: An Instrument to Measure Snow Optically Equivalent Grain Size, *IEEE Transactions on Geoscience and Remote Sensing*, *52*(7), 4236–4247, doi:10.1109/TGRS.2013.2280502.

Hadley, O. L., and T. W. Kirchstetter (2012), Black-carbon reduction of snow albedo, *Nature Climate Change*, *2*(6), 437–440, doi:10.1038/nclimate1433.

Hall, A. (2004), The Role of Surface Albedo Feedback in Climate, *Journal of Climate*, *17*(7), 1550–1568, doi:10.1175/1520-0442(2004)017¡1550:TROSAF¿2.0.CO;2.

Hall, A., and X. Qu (2006), Using the current seasonal cycle to constrain snow albedo feedback in future climate change, *Geophysical Research Letters*, *33*(3), doi:10.1029/2005GL025127.

Held, I. M., and M. J. Suarez (1974), Simple albedo feedback models of the icecaps, *Tellus*, *26*(6), 613–629, doi:10.1111/j.2153-3490.1974.tb01641.x.

Hudson, S. R. (2011), Estimating the global radiative impact of the sea icealbedo feedback in the Arctic, *Journal of Geophysical Research*, *116*(D16), doi:10.1029/2011JD015804.

Hudson, S. R., S. G. Warren, R. E. Brandt, T. C. Grenfell, and D. Six (2006), Spectral bidirectional reflectance of Antarctic snow: Measurements and parameterization, *Journal of Geophysical Research*, *111*(D18), doi:10.1029/2006JD007290.

Jin, Z., T. P. Charlock, P. Yang, Y. Xie, and W. Miller (2008), Snow optical properties for different particle shapes with application to snow grain size retrieval and MODIS/CERES radiance comparison over Antarctica, *Remote Sensing of Environment*, *112*(9), 3563–3581, doi:10.1016/j.rse.2008.04.011.

Kaempfer, T. U., M. A. Hopkins, and D. K. Perovich (2007), A three-dimensional microstructure-based photon-tracking model of radiative transfer in snow, *Journal of Geophysical Research*, *112*(D24), doi:10.1029/2006JD008239.

Kay, J. E., B. R. Hillman, S. A. Klein, Y. Zhang, B. Medeiros, R. Pincus, A. Gettelman, B. Eaton, J. Boyle, R. Marchand, and T. P. Ackerman (2012), Exposing Global Cloud Biases in the Community Atmosphere Model (CAM) Using Satellite Observations and Their Corresponding Instrument Simulators, *Journal of Climate*, *25*(15), 5190–5207, doi:10.1175/JCLI-D-11-00469.1.

Kopp, G., and J. L. Lean (2011), A new, lower value of total solar irradiance: Evidence and climate significance: FRONTIER, *Geophysical Research Letters*, *38*(1), n/a–n/a, doi:10.1029/2010GL045777.

Kwok, R., and D. A. Rothrock (2009), Decline in Arctic sea ice thickness from submarine and ICESat records: 1958-2008: ARCTIC SEA ICE THICKNESS, *Geophysical Research Letters*, *36*(15), n/a–n/a, doi:10.1029/2009GL039035.

Legagneux, L., and F. Domine (2005), A mean field model of the decrease of the specific surface area of dry snow during isothermal metamorphism: MODEL OF SNOW SURFACE AREA DECREASE, *Journal of Geophysical Research: Earth Surface*, *110*(F4), n/a–n/a, doi:10.1029/2004JF000181.

Legagneux, L., A. Cabanes, and F. Domin (2002), Measurement of the specific surface area of 176 snow samples using methane adsorption at 77 K: MEASUREMENT USING METHANE ADSORPTION AT 77 K, *Journal of Geophysical Research: Atmospheres*, *107*(D17), ACH 5–1–ACH 5–15, doi:10.1029/2001JD001016.

Legagneux, L., A.-S. Taillandier, and F. Domine (2004), Grain growth theories and the isothermal evolution of the specific surface area of snow, *Journal of Applied Physics*, *95*(11), 6175–6184, doi:10.1063/1.1710718.

Libois, Q., G. Picard, L. Arnaud, M. Dumont, M. Lafaysse, S. Morin, and E. Lefebvre (2015), Summertime evolution of snow specific surface area close to the surface on the Antarctic Plateau, *The Cryosphere*, *9*(6), 2383–2398, doi:10.5194/tc-9-2383-2015.

Mountain Research Initiative EDW Working Group (2015), Elevation-dependent warming in mountain regions of the world, *Nature Climate Change*, *5*(5), 424–430, doi:10.1038/nclimate2563.

North, G., and K.-Y. Kim (2015), CLIMATE AND CLIMATE CHANGE | Energy Balance Climate Models, in *Encyclopedia of Atmospheric Sciences*, pp. 69–72, Elsevier, doi:10.1016/B978-0-12-382225-3.00001-3.

North, G. R. (1975), Theory of Energy-Balance Climate Models, *Journal of the Atmospheric Sciences*, *32*(11), 2033–2043, doi:10.1175/1520-0469(1975)032¡2033:TOEBCM¿2.0.CO;2.

Painter, T. H., N. P. Molotch, M. Cassidy, M. Flanner, and K. Steffen (2007), Contact spectroscopy for determination of stratigraphy of snow optical grain size, *Journal of Glaciology*, *53*(180), 121–127, doi:10.3189/172756507781833947.

Painter, T. H., K. Rittger, C. McKenzie, P. Slaughter, R. E. Davis, and J. Dozier (2009), Retrieval of subpixel snow covered area, grain size, and albedo from MODIS, *Remote Sensing of Environment*, *113*(4), 868–879, doi:10.1016/j.rse.2009.01.001.

Perket, J., M. G. Flanner, and J. E. Kay (2014), Diagnosing shortwave cryosphere radiative effect and its 21st century evolution in CESM: SHORTWAVE CRYOSPHERE RADIATIVE EFFECT, *Journal of Geophysical Research: Atmospheres*, *119*(3), 1356–1362, doi:10.1002/2013JD021139.

Picard, G., L. Arnaud, F. Domine, and M. Fily (2009), Determining snow specific surface area from near-infrared reflectance measurements: Numerical study of the influence of grain shape, *Cold Regions Science and Technology*, *56*(1), 10–17, doi:10.1016/j.coldregions.2008.10.001.

Pinzer, B. R., and M. Schneebeli (2009), Snow metamorphism under alternating temperature gradients: Morphology and recrystallization in surface snow, *Geophysical Research Letters*, *36*(23), doi:10.1029/2009GL039618.

Pistone, K., I. Eisenman, and V. Ramanathan (2014), Observational determination of albedo decrease caused by vanishing Arctic sea ice, *Proceedings of the National Academy of Sciences*, *111*(9), 3322–3326, doi:10.1073/pnas.1318201111.

Pithan, F., and T. Mauritsen (2014), Arctic amplification dominated by temperature feedbacks in contemporary climate models, *Nature Geoscience*, *7*(3), 181–184, doi:10.1038/ngeo2071.

Qian, Y., T. J. Yasunari, S. J. Doherty, M. G. Flanner, W. K. M. Lau, J. Ming, H. Wang, M. Wang, S. G. Warren, and R. Zhang (2015), Light-absorbing particles in snow and ice: Measurement and modeling of climatic and hydrological impact, *Advances in Atmospheric Sciences*, *32*(1), 64–91, doi:10.1007/s00376-014-0010-0.

Qu, X., and A. Hall (2006), Assessing Snow Albedo Feedback in Simulated Climate Change, *Journal of Climate*, *19*(11), 2617–2630, doi:10.1175/JCLI3750.1.

Qu, X., and A. Hall (2007), What Controls the Strength of Snow-Albedo Feedback?, *Journal of Climate*, *20*(15), 3971–3981, doi:10.1175/JCLI4186.1.

Qu, X., and A. Hall (2014), On the persistent spread in snow-albedo feedback, *Climate Dynamics*, *42*(1-2), 69–81, doi:10.1007/s00382-013-1774-0.

Ramanathan, V., and G. Carmichael (2008), Global and regional climate changes due to black carbon, *Nature Geoscience*, *1*(4), 221–227, doi:10.1038/ngeo156.

Roberts, J., and T. D. Roberts (1978), Use of the Butterworth low-pass filter for oceanographic data, *Journal of Geophysical Research*, *83*(C11), 5510, doi:10.1029/JC083iC11p05510.

Schneider, A., M. Flanner, and J. Perket (2018), Multidecadal Variability in Surface Albedo Feedback Across CMIP5 Models, *Geophysical Research Letters*, *45*(4), 1972–1980, doi:10.1002/2017GL076293.

Sellers, W. D. (1969), A Global Climatic Model Based on the Energy Balance of the Earth-Atmosphere System, *Journal of Applied Meteorology*, *8*(3), 392–400, doi:10.1175/1520-0450(1969)008¡0392:AGCMBO¿2.0.CO;2.

Shell, K. M., J. T. Kiehl, and C. A. Shields (2008), Using the Radiative Kernel Technique to Calculate Climate Feedbacks in NCARs Community Atmospheric Model, *Journal of Climate*, *21*(10), 2269–2282, doi:10.1175/2007JCLI2044.1.

Skiles, S. M., and T. Painter (2017), Daily evolution in dust and black carbon content, snow grain size, and snow albedo during snowmelt, Rocky Mountains, Colorado, *Journal of Glaciology*, *63*(237), 118–132, doi:10.1017/jog.2016.125.

Soden, B. J., and I. M. Held (2006), An Assessment of Climate Feedbacks in Coupled OceanAtmosphere Models, *Journal of Climate*, *19*(14), 3354–3360, doi:10.1175/JCLI3799.1.

Soden, B. J., I. M. Held, R. Colman, K. M. Shell, J. T. Kiehl, and C. A. Shields (2008), Quantifying Climate Feedbacks Using Radiative Kernels, *Journal of Climate*, *21*(14), 3504–3520, doi:10.1175/2007JCLI2110.1.

Stroeve, J., M. M. Holland, W. Meier, T. Scambos, and M. Serreze (2007), Arctic sea ice decline: Faster than forecast: ARCTIC ICE LOSS-FASTER THAN FORECAST, *Geophysical Research Letters*, *34*(9), doi:10.1029/2007GL029703.

Stroeve, J. C., M. C. Serreze, M. M. Holland, J. E. Kay, J. Malanik, and A. P. Barrett (2012), The Arctics rapidly shrinking sea ice cover: a research synthesis, *Climatic Change*, *110*(3-4), 1005–1027, doi:10.1007/s10584-011-0101-1.

Taylor, K. E., R. J. Stouffer, and G. A. Meehl (2012), An Overview of CMIP5 and the Experiment Design, *Bulletin of the American Meteorological Society*, *93*(4), 485–498, doi:10.1175/BAMS-D-11-00094.1.

Vial, J., J.-L. Dufresne, and S. Bony (2013), On the interpretation of inter-model spread in CMIP5 climate sensitivity estimates, *Climate Dynamics*, *41*(11-12), 3339–3362, doi:10.1007/s00382-013-1725-9.

Vouk, V. (1948), Projected Area of Convex Bodies, *Nature*, *162*(4113), 330–331, doi:10.1038/162330a0.

Wang, M., and J. E. Overland (2012), A sea ice free summer Arctic within 30 years: An update from CMIP5 models: SUMMER ARCTIC SEA ICE, *Geophysical Research Letters*, *39*(18), doi:10.1029/2012GL052868.

Wang, X., and I. Baker (2014), Evolution of the specific surface area of snow during high-temperature gradient metamorphism, *Journal of Geophysical Research: Atmospheres*, *119*(24), 13,690–13,703, doi:10.1002/2014JD022131.

Warren, S. G., and W. J. Wiscombe (1980), A Model for the Spectral Albedo of Snow. II: Snow Containing Atmospheric Aerosols, *Journal of the Atmospheric Sciences*, *37*(12), 2734–2745, doi:10.1175/1520-0469(1980)037¡2734:AMFTSA¿2.0.CO;2.

Winton, M. (2006a), Amplified Arctic climate change: What does surface albedo feedback have to do with it?, *Geophysical Research Letters*, *33*(3), doi:10.1029/2005GL025244.

Winton, M. (2006b), Surface Albedo Feedback Estimates for the AR4 Climate Models, *Journal of Climate*, *19*(3), 359–365, doi:10.1175/JCLI3624.1.

Wiscombe, W. J., and S. G. Warren (1980), A Model for the Spectral Albedo of Snow. I: Pure Snow, *Journal of the Atmospheric Sciences*, *37*(12), 2712–2733, doi:10.1175/1520-0469(1980)037¡2712:AMFTSA¿2.0.CO;2.

Yang, P., L. Bi, B. A. Baum, K.-N. Liou, G. W. Kattawar, M. I. Mishchenko, and B. Cole (2013), Spectrally Consistent Scattering, Absorption, and Polarization Properties of Atmospheric Ice Crystals at Wavelengths from 0.2 to 100 m, *Journal of the Atmospheric Sciences*, *70*(1), 330–347, doi:10.1175/JAS-D-12-039.1.